1st printing

Diode Lasers Errata	page	location	Error	Correction
Chapter 1				
Chapter 2	65	Figure 2.10	Gamma_g_0 tangent at e*Ntr	
	82	Example 2.5, last equation	missing * between 250 and 10^-4	add *
Chapter 3	104	Example 3.1, paragraph after second equation	\phi_2 = \beta_1*L_1	\phi_2 = \beta_2*L_2
	119	Paragraph above eq 3.57	1.88	1.90
	119	Eq. 3.57	3.76	3.8
Chapter 4	179	unlabeled equation above "quantum dots"	(g*f2 - f1)	g*(f2 - f1)
	216	Example 4.6		PDF corrected
	231	5th line of text	"Althoug" misspelled	"Although"
	237	Example 4.9,		see PDF
	238	Example 4.9,		see PDF
Chapter 5	259	Para after Eq. 5.36	(5.38)	(5.36)
	262	Second paragraph from bottom	\omega_{3 db), 3 instances in this paragraph	remove spacing between 3 and dB in subscript, should be 3dB
	281	Eq. (5.88)	summations N, N	should be M, N
	296	Paragraph before section "Characteristics of the RIN Spectrum"	Reference to Eq. 5.130	Should reference to Eq. 5.139
	321	Eq 5.200	dN_p	should be dN (remove p in subscript)
	321	Paragraph after (5.201)	N_th	should be italicized
	330	Problem 2	Misspelling "instread"	instead
Chapter 6	336	Last line of page	Cites Figure 11.1	Should be Figure A3.1
	337	Sentence before Eq 6.7	E_x and H_y	Should be E_y and H_x
	337	Eq.(6.7)	E_x	E_y, both instances
	338	second paragraph from bottom	"of the previous chapter"	"of this chapter"
	342	Last sentence	Section 14.2	Example 6.1
	356	First line of paragraph following eq 6.58	t_2' = r_2	t_2' = t_2

	360	Paragraph below Eq. 6.68	Mispelled "slighltly"	Should be "slightly"
	361	Eq.6.72	k_12 and k_21	replace "k" by \kappa
	362	last equation in example 6.4	-0.192	-1.192
	365	Paragraph below Eq. 6.85	Mispelled "jaron"	Should be "jargon"
	369	paragraph before last equation on this page	e^-(10x0.25)	e^-(10x0.025)
	375	Example 6.8, last equation on page	n_g	missing capital Delta before n_g, Delta*n_g
	375	First sentence	6.21	6.20
	378	Paragraph above Fig 6.23	'general' and 'restricted' begin with an italicized letter	italicize whole words "general" and "restricted"
	380	Paragraph after equation 6.103	Eq. (6.55).	should be Eq.(6.13)
	381	Section 6.7, first paragraph	Misspelled "difraction"	should be "diffraction"
	382	First paragraph	Misspelled "difracted"	should be "diffracted"
	385	Last paragraph	Misspelled "depeding"	should be "depending"
	387	Top paragraph	Mispelled : 'detemined'	should be 'determined'
	389	Section 6.8.2, first paragraph	misspelled "difracts"	should be "diffracts"
Chapter 7	400	Example 7.1, solution, first paragraph of part (b)	y_tx	\gamma_tx
	400	last equation in example 7.1	3.4	1.163
	400	last equation in example 7.1	25.37nm	70.1nm
	402	Paragraph below eq 7.17	Reference to Eq (11.10) in Appendix 3	A3.10
	403	example 7.2, second equation	25.37nm	70.1nm
	403	example 7.2, last equation	50.74nm	140.2nm
	403	example 7.2, last equation	717nm	807nm
	410	Example 7.3, last row	3.221	3.218
	413	Eq. 7.32	sign =	replace by -

	447	Problem 7.7	reads 4.0<d<1.0	Should read 1.0<d<4.0
	449	Problem 7.14	2.3	should be 2.2
	462	second equation on this page	a factor "2" is missing in the denominator (bottom) of the second fraction	insert "2 * " in front of "Leff"
Chapter 8	464	Figure 8.7	missing labels on abscissae	insert \lambda symbol
	465	example 8.3		see pdf
	465	example 8.3		see pdf
	472	section (b) in example	Eq.(6.44)	should be Eq.(6.92)
	482	3lines after (8.12)	in g0=a[eti-i I tau/...]	tau is not a subscript
	500	Reference 14	laset	should be "laser"
	505	Problem 8.8	delta n/n	n in delta n should have a bar over it
	506	Problem 9. third row	"shihers"	should be "shifters"
	507	Problem 9. part (e)	misspelled "cunent"	should be "current"
Appendix 15	678	After equation A15.1	Chapter 7	should be Chapter 6

Corrections for *Diode Lasers and Photonic Integrated Circuits*—**Summary**

(See also attached text screen shots with corrections & PPT figures)

Page	Correction
16	Italicize "*two-thirds of the band offset*" in 11th line of 1st paragraph Italicize "*about 40% of the band offset*" in last sentence of 2nd paragraph Italicize "*conduction band offset of* $\Delta E_c = 0.7\Delta E_g$." in 11th line of 3rd paragraph
70	All equations ≥ 2.47 need to be increased by 6. Any reference to these equations also changes, except imbedded references on pp 80, 81, & 82 to (2.49), (2.50). & (2.52)
73	Example 2.3, line #5 from bottom, "Differential gain/alpha can be computed using expression Eq. (2.46)" ---> it should be Eq. (2.47) (the first 2.47, not the duplicated 2.47)
74	Example equation for f_R, last factor, replace (0.3) by (0.03)
77	Last line, the bracket ")" before "= 15 cm^{-1}" should be removed.
90	For #15. Second line, replace 'Problem 2.15' by "Problem 2.14"
109	Line 2 below Eq. (3.40), "reducing ...to Eq. (2.29)" --> should be Eq. (2.32)
133	Last equation r'gb should actually be r'gt
134	Equation for η_d near top, --replace 0.349 by 0.823 --remove square root signs after 'ln' in numerator and denominator --replace 10^{-8} by 10^{-7} in denominator --replace 0.703 by 0.584 on far right
138	Second equation, $\Delta\lambda_m$, remove '2' from denominator in first line - Replace '0.277 nm' by "0.453 nm" in second line Third equation, $\Delta\lambda_{lasing}$, replace '0.277' by "0.453" after second = sign - Replace '4.439' by "4.665" on far right
144	*Replace Page with one supplied—mount sideways (attached PPT is camera-ready): existing bottom graph has vertical scale erroneously expanded relative to data and is too small to read
145	In figure caption, sixth line, change subscript from '*g*' to "*a*" to read "...ΔL_a,"

146 **Replace Page with one supplied—mount sideways (attached PPT is camera-ready): existing bottom graph has vertical scale erroneously expanded relative to data and is too small to read

148 --Bottom equation is incorrect, and graph is read incorrectly. Last sentence, replace '0.35' by "-1.8". Replace 'β = ...' first equation line by:

$$\Delta\lambda = -\frac{\lambda_0^2 \delta}{2\pi n_g}$$

--Replace second line by:

$$\Delta\lambda = -\frac{1.55^2}{2\pi \cdot 3.8}\frac{(-1.8)}{(500)} = 0.362\times10^{-3}\,\mu\text{m} \Longrightarrow \quad \lambda = 1550.362\ \text{nm}$$

179 Equation after 1st paragraph: after '>' on right, 2nd parenthesis misplaced; should be:

" $> g_{max1}(E_{g1})(f_2(E_{c1}) - f_1(E_{v1}))$."

190 Equations (4.55 – 4.58) have errors—(4.54) is ok:

$c \approx 10 - 20$ meV/$(10^{12}$ cm$^{-2})^{1/2}$.	(GaAs/AlGaAs QW)	(4.55)
$c \approx 20 - 25$ meV/$(10^{12}$ cm$^{-2})^{1/2}$.	(InGaAs/InP QW)	(4.56)
$c \approx 2 - 2.2$ meV/$(10^{8}$ cm$^{-2})^{1/2}$.	(GaN/AlGaN QW)	(4.57)
$c \approx 2 - 2.2$ meV/$(10^{8}$ cm$^{-2})^{1/2}$.	(InGaN/GaN QW)	(4.58)

190 Paragraph immediately after Equations (4.54 – 4.58) needs to be modified.
--In the second line, delete "one-third".
--At the end of the paragraph add "using bulk actives," so that it ends with, " ...for the GaAs/AlGaAs system using bulk actives."

195 Text after Equation (4.69): change reference from Eq. (4.33) to (4.38), and from (4.48) to (4.66).
r'gb I highlighted above should actually be r'gt

197 --Next to last line on page in equation for $P_{sptotal}$, should have an additional factor on far right of: $\cdot\ 1.6\cdot10^{-19}$ J/eV
--Last line, the answer should be 53.5 µW.

209 In **Solution**, first line, (4.111) should be (4.87)

216 Last line of Example problem solution is incorrect. It should be:

$$C(340\text{K}) = C(300\text{K}) \cdot e^{-\frac{80}{26}\frac{300}{340}+\frac{80}{26}} = 1.436 \cdot C(300\text{K}) = 8.167 \cdot 10^{-29}\ \text{cm}^6/\text{s}.$$

*This could also be written as:

$$C(340\text{K}) = C(300\text{K}) \cdot \exp\left[-\frac{80}{26}\frac{300}{340} + \frac{80}{26}\right] = 1.436 \cdot C(300\text{K}) = 8.167 \cdot 10^{-29}\ \text{cm}^6/\text{s}.$$

226 **Example 4.7**, six lines up from bottom, equation: V = ..., 'cm^{-3}' should be "cm^3" in two places—i.e., no minus sign in exponent
--Also, four lines up, equation: I_{th} = ..., same correction, 'cm^{-3}' should be "cm^3"

232 **Example 4.8**, end of first paragraph, change 'Example 4.5' to "Fig. 4.31: C = 6e-29 cm^6/s."
--Also, five lines up from bottom, parenthesis containing '$6.32 \cdot 10^{18}$ cm^{-3}' should be cubed, so that it becomes: "$(6.32 \cdot 10^{18}\ cm^{-3})^3$"

237 Last line of text, should have a " -1" in second quantity:
$\Delta I_A = (1.1)^3 \cdot (1.436 - 1) I_A$. Finally,

238 Answer to Example problem should be 67 K, not 70 K.

244 Last line, should be Fig. 4.20 not 4.18

274 Third line in text below Eqns. (5.79), 'well-plug' should be "wall-plug"

293 After Equation (5.122) in text, replace (5.113) with (5.121), and replace (5.112) with (5.122).

309 In Equation (5.165), lower-right equation should have lower-case 'gamma' on right side:
$\gamma_{tNN} = \gamma_{NN} + 1/\tau_e$

337 --Third line after Equation (6.6), change x to y-direction:
"...aligned along the y-direction."
--Fourth line after Equation (6.6), change subscripts:
"... and $\mathcal{H}_x = (j/\omega\mu) d\mathcal{E}_y/dz$, we have"

--Equation (6.8) change subscript from x to y:
$\mathcal{E}_y$ = ...

365 Equation at top—denominator factor is incorrect—should be 0.0681, not 0.0659:
$L_c \equiv \frac{\pi}{2\kappa} = \frac{\pi}{2(0.0681 \mu m^{-1})} = 23.1\ \mu m$

367 Line 2 above Example 6.7. "priciple" should be "principle"

421 In center of page beneath equations, change A3.12 to A3.2.

495 Second line of Equation(8.23), add prefactor of, $\frac{q\eta}{h\nu}$, and enclose existing left side in brackets: That is,

$$= \frac{q\eta}{h\nu}\left[P_{LO} + P_{IN} + 2\sqrt{P_{LO}P_{IN}}\cos\left((\omega_{IN} - \omega_{LO})t \pm \Phi_{IN} \mp \Phi_{LO}\right)\right]$$

504 Third line from top, change 'internal efficiency' to "injection efficiency."
At end of Prob. #2 first paragraph, add sentence: "Assume width of 3μm."

Bottom of page: Same change from 'internal' to "injection" in Prob. #5, next to last line.

506 At the end of Prob. #9 first paragraph add sentence: "Other gain, loss, tuning, efficiency, and index parameters are identical to those given in Problem #8."

563 Add another paragraph before the last one as follows:

Of course, (A4.10) was derived assuming a relatively large homogeneous optical cavity, beginning with the simple boundary conditions (A4.1), and no smaller sized, higher-index 'active region' was assumed within its contents. In problems of interest, there is such an active region that confines from one to a few modes closely to this region. However, since there are typically hundreds to hundreds-of-thousands of modes in total, these few do not measurably change the derivation of (A4.10), although the value of β_{sp} is significantly larger for these confined modes, because $\Gamma_c \rightarrow \Gamma$ is larger for them.

676 The three equation numbers should be incremented by one after equations:
(A14.1) → (A14.2)
(A14.2) → (A14.3)
(A14.3) → (A14.4)

676 In the text, only the reference to Eq. (A14.2) in the bottom paragraph should be changed to (A14.3)

676 First line after Equation (A14.1), replace (A14.1) with (6.19).

CORRECTIONS IN RED ADDED 6/13/2016; OTHERS REMAIN THE SAME AS SUMMITTED 1/29/2016

**LAST UPDATED 2/2021

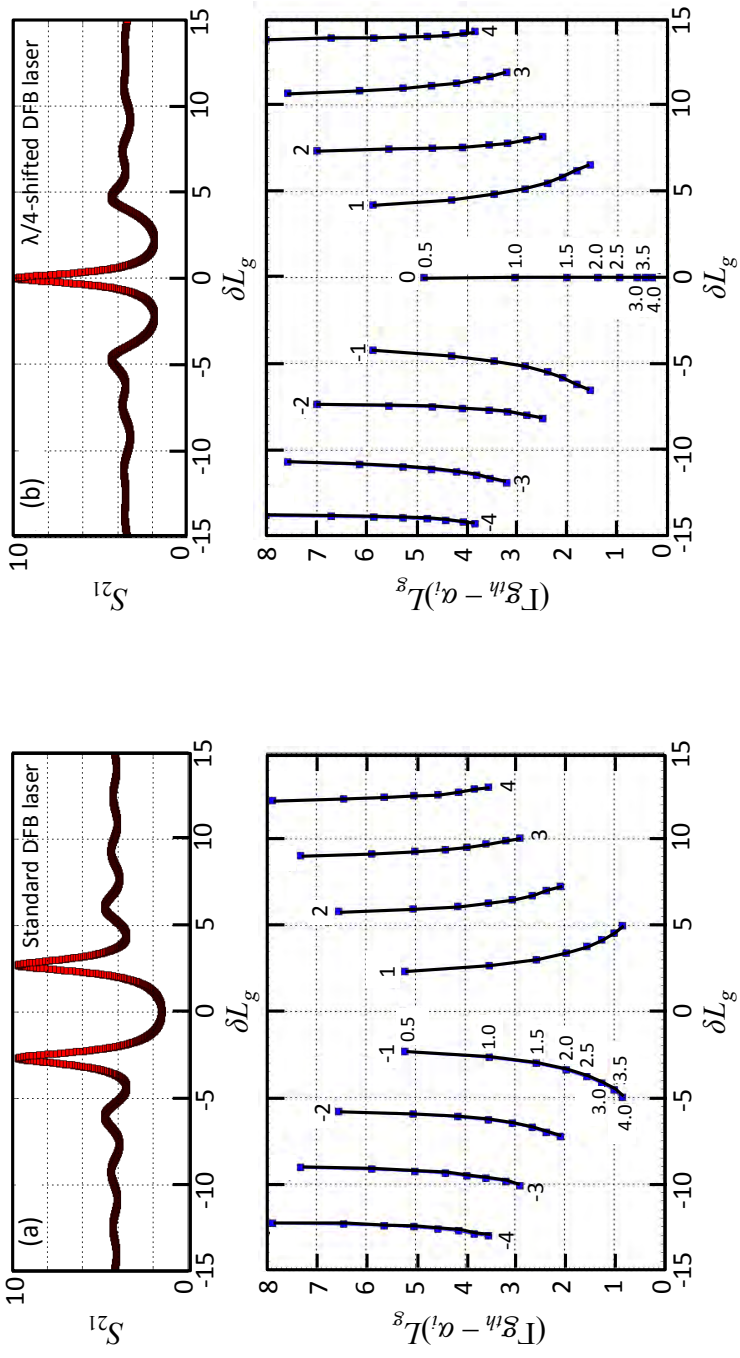

FIGURE 3.26: Example S_{21} spectra and normalized plots of threshold modal gain and threshold wavelength for different modes of (a) standard and (b) quarter-wave shifted DFB lasers. S_{21} spectra shown for $\kappa L_g = 1$ at a gain just below threshold; plots summarize analogous threshold points for this lowest order and some higher order modes with κL_g ($\equiv 2mr$) ranging from 0.5 to 4 in 0.5 increments. Here $\delta = \beta - \beta_0$, where β is the average propagation constant of the grating.

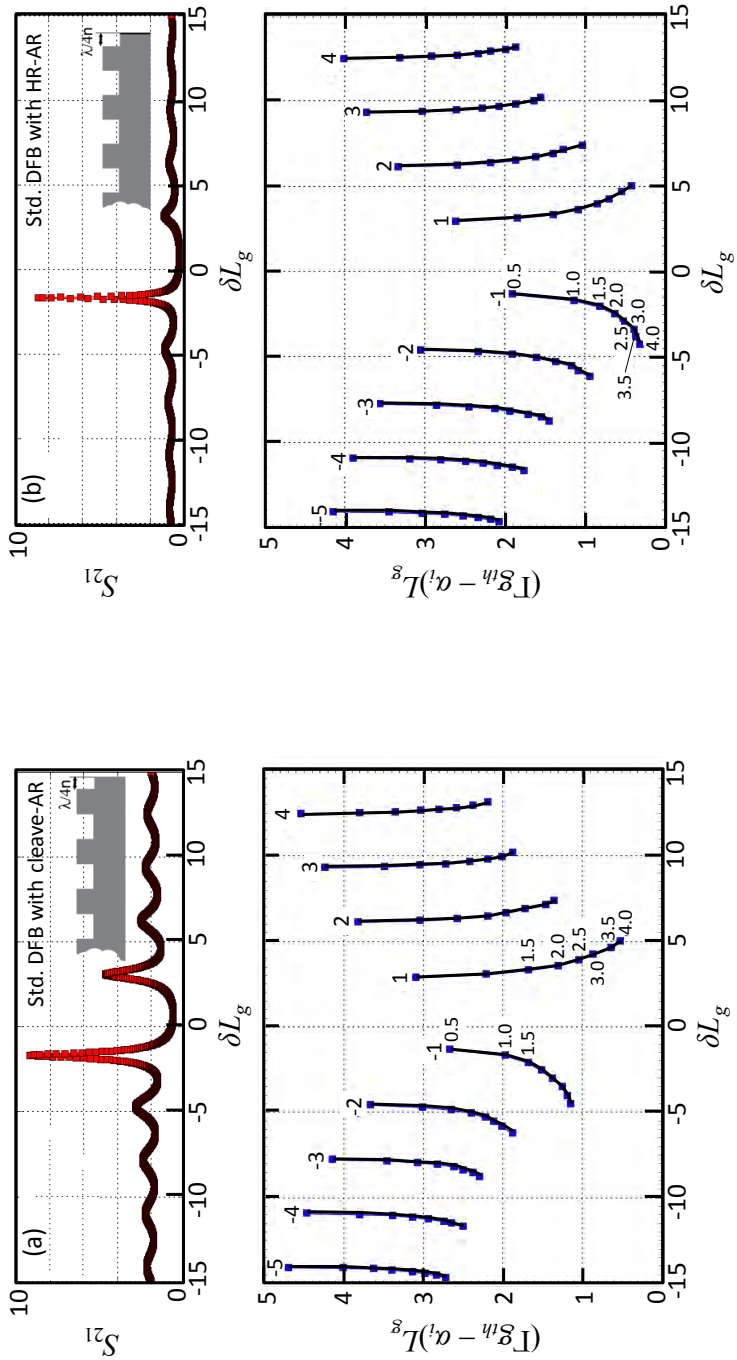

FIGURE 3.28: Example S_{21} spectra and normalized plots of threshold modal gain and threshold wavelength for different modes of a standard DFB laser with one end AR-coated and the other end either (a) a simple cleave, $R = 0.32$, or (b) HR-coated with $R = 0.9$. S_{21} spectra shown for $\kappa L_g = 1$ at a gain just below threshold; plots summarize analogous threshold points for this lowest order and some higher order modes with κL_g ($\equiv 2m\pi$) ranging from 0.5 to 4 in 0.5 increments. The additive end reflections are optimally placed to provide orthogonally phased reflections (as illustrated by the insets).

be adjusted somewhat without changing the lattice constant. Thus, in general, a quaternary compound is required in a DH laser to allow the adjustment of the energy gap while maintaining lattice matching. Fortunately, there are some unique situations that allow the use of more simple ternaries. As can be seen, the AlGaAs ternary line is almost vertical. That is, the substitution of Al for Ga in GaAs does not change the lattice constant very much. Thus, if GaAs is used as the substrate, any alloy of $Al_xGa_{1-x}As$ can be grown, and it will naturally lattice match, so that no misfit dislocations or other defects should form. As suggested by the formula, the x-value determines the percentage of Al in the group III half of the III–V compound. The AlGaAs/GaAs system provides lasers in the 0.7–0.9 μm wavelength range. For DH structures in this system, about two-thirds of the band offset occurs in the conduction band. For shorter wavelengths into the red (e.g., 650 nm as used in DVDs), the AlInGaP/GaAs system is generally employed. In this case lattice matching requires a precise control of the ratios of Al:In:Ga in the quaternary regions.

The most popular system for long-distance fiber optics is the InGaAsP/InP system. Here the quaternary is specified by an x and y value (i.e., $In_{1-x}Ga_xAs_yP_{1-y}$). This is grown on InP to form layers of various energy gap corresponding to wavelengths in the 1.0–1.6 μm range, where silica fiber traditionally had minima in loss (1.55 μm) and dispersion (1.3 μm). Using InP as the substrate, a range of lattice-matched quaternaries extending from InP to the InGaAs ternary line can be accommodated, as indicated by the vertical line in Fig. 1.9. Fixing the quaternary lattice constant defines a relation between x and y. It has been found that choosing x equal to $\sim 0.47y$ results in approximate lattice matching to InP. The ternary endpoint is $In_{0.53}Ga_{0.47}As$. For DH structures in this system, only about 40% of the band offset occurs in the conduction band.

InGaAsP lasers and photonic integrated circuits (PICs) generally need to be operated at a constant temperature to maintain their performance. This is primarily due to the fact that with the increasing temperature, the electron leakage current from the quantum well increases. The main material parameter controlling the current leakage is the conduction band offset. Due to their much lighter effective mass, electrons require much tighter confinement with increasing temperature than holes. To improve the diode laser performance at high temperatures, particularly of interest for the fiber-optic metropolitan area network deployment, material engineering was successfully employed to increase the conduction band offset, through introduction of InGaAlAs material system. This material system enables quantum wells with the conduction band offset of $\Delta E_c = 0.7\Delta E_g$. Changing the barrier from $\Delta E_c = 0.4\Delta E_g$ to $\Delta E_c = 0.7\Delta E_g$ will lead to the reduction of the leakage current density from $J = 50$ A/cm^2 to $J = 1.5$ A/cm^2. Uncooled operation of lasers and integrated laser electroabsorption modulator PICs have been demonstrated at both 1310 nm and 1550 nm, and this remains an active area of research and deployment.

Lattice constants of ternary and quaternary compounds can be precisely calculated from Vegard's law, which gives a value equal to the weighted average of all the four possible constituent binaries. For example, in $In_{1-x}Ga_xAs_yP_{1-y}$, we

quantum wells, as indicated by the gain parameters listed after Eq. (2.46). If such higher-order nonradiative carrier recombination is important at threshold, one must add another component to the threshold current due to the CN_{th}^3 term in the recombination rate. Then, Eqs. (2.49) and (2.50) should be increased by

$$I_{nrth} = \frac{qVCN_{tr}^3}{\eta_i} e^{3(\langle\alpha_i\rangle+\alpha_m)/\Gamma g_0}, \tag{2.52}$$

where for 1.3 μm InGaAsP material, the Auger coefficient, $C \sim 3 \times 10^{-29}$ cm^6/s, and for 1.55 μm material it is about two or three times larger. The cubic dependence on N_{th} places more importance on reducing the threshold carrier density in this material system. In fact, this additive Auger term dominates Eq. (2.49) for carrier densities above $N_{th} \sim 3 \times 10^{18}$ or 1.5×10^{18} cm^{-3} at 1.3 and 1.55 μm, respectively. This fact focuses more attention on reducing cavity losses, $(\langle\alpha_i\rangle + \alpha_m)$, and maintaining a large confinement factor, Γ. With the use of strained-layer InGaAs/InGaAsP or InGaAs/InGaAlAs quantum wells on InP, a considerable improvement is possible because all the parameters affecting N_{th} move in the right direction. In fact, the Auger coefficient, C, may also be reduced due to the splitting of the valence bands.

2.7 RELAXATION RESONANCE AND FREQUENCY RESPONSE

Chapter 5 will discuss dynamic effects in some detail. Here, we wish to use Eqs. (2.16) and (2.17) to briefly outline the calculation of relaxation resonance frequency and its relationship to laser modulation bandwidth. As shown in Chapter 5, because of gain compression with increasing photon density and possible transport effects, the calculations are a bit oversimplified, particularly with respect to quantum-well structures. However, these simple equations do seem to work well for standard DH structures, and the method of attack for calculating resonance frequency is also instructive for the more complex calculations to follow in Chapter 5.

Consider the application of an above-threshold DC current, I_0, superimposed with a small AC current, I_1, to a diode laser. Then, under steady-state conditions the laser's carrier density and photon density would respond similarly, with some possible harmonics of the drive frequency, ω, that we shall ignore. Using complex frequency domain notation,

$$I = I_0 + I_1 e^{j\omega t}, \tag{2.47a}$$

$$N = N_0 + N_1 e^{j\omega t}, \tag{2.47b}$$

$$N_p = N_{p0} + N_{p1} e^{j\omega t}. \tag{2.47c}$$

Before applying these to Eqs. (2.16) and (2.17), we first rewrite the rate equations using $g = a\Delta N$ for the gain. This is valid because small-signal conditions are assumed, and the gain can be well approximated by a linear

deviation from its steady-state value, g_{th}, over some small range of carrier densities, ΔN, *provided the local slope*, $a = \partial g/\partial N$, at the bias point N_0 is used. We also assume the DC current is sufficiently far above threshold that the spontaneous emission can be neglected. That is,

$$\frac{dN}{dt} = \frac{\eta_i I}{qV} - \frac{N}{\tau} - v_g(g_{th} + a\Delta N)N_p, \tag{2.54}$$

$$\frac{dN_p}{dt} = \Gamma v_g(g_{th} + a\Delta N)N_p - \frac{N_p}{\tau_p}. \tag{2.55}$$

Now, after plugging in Eq. (2.47) for I, N, and N_p, we note that $\Delta N \equiv N_1 \exp(j\omega t)$ and recognize that the DC components satisfy the steady-state versions of Eqs. (2.48) and (2.49) (i.e., with $d/dt \to 0$); and they can be grouped together and set to zero. Next, we recognize that the steady-state gains, g_{th}, can be replaced by $[\Gamma v_g \tau_p]^{-1}$ according to Eq. (2.28). Finally, we delete the second-harmonic terms that involve $e^{j2\omega t}$ and divide out an $e^{j\omega t}$ common factor. Then,

$$j\omega N_1 = \frac{\eta_i I_1}{qV} - \frac{N_1}{\tau} - \frac{N_{p1}}{\Gamma\tau_p} - v_g a N_1 N_{p0}, \tag{2.56}$$

$$j\omega N_{p1} = \Gamma v_g a N_1 N_{p0}. \tag{2.57}$$

With the preceding manipulations we have generated frequency domain equations that can easily be solved for the transfer function $N_{p1}(\omega)/I_1(\omega)$. First, solving for N_1 in Eq. (2.51), we have $N_1 = j\omega N_{p1}/\Gamma v_g a N_{p0}$. Then eliminating N_1 from Eq. (2.50) and using $P_{ac} = v_g \alpha_m N_{p1} h\nu V_p$, we obtain

$$\frac{P_{ac}(\omega)}{I_1(\omega)} = \frac{\eta_i h\nu}{q} \frac{v_g \alpha_m (v_g a N_{p0})}{v_g a N_{p0}/\tau_p - \omega^2 + j\omega[v_g a N_{p0} + 1/\tau]}. \tag{2.58}$$

Now we observe that the first term in the denominator is the square of a natural resonance frequency, so we define,

$$\omega_R^2 \equiv \frac{v_g a N_{p0}}{\tau_p}. \tag{2.59}$$

Using Eqs. (2.28) and (2.40), the transfer function can be written in a more normalized form:

$$\frac{P_{ac}(\omega)}{I_1(\omega)} = \frac{\eta_d h\nu/q}{1 - (\omega/\omega_R)^2 + j(\omega/\omega_R)[\omega_R\tau_p + 1/\omega_R\tau]}. \tag{2.60}$$

For sufficiently low modulation frequencies, the denominator reduces to one and Eq. (2.54) reduces to the AC equivalent of Eq. (2.41). For higher modulation frequencies, the $1 - (\omega/\omega_R)^2$ term in the denominator creates a strong resonance in the response. Figure 2.13 illustrates the frequency dependence for a wide range

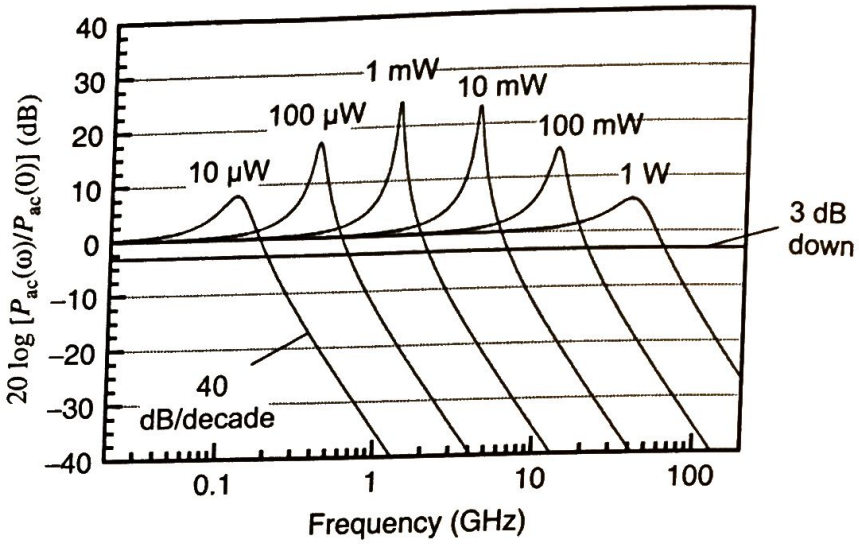

FIGURE 2.13: Frequency response of an idealized diode laser for several different output powers. The active region is characterized by: $h\nu = 1.5$ eV, $a = 5 \times 10^{-16}$ cm^2, $\tau = 3 \times 10^{-9}$ s, $\eta_i = 86.7\%$, and $v_g = 3 \times 10^{10}/4$ cm/s. The laser cavity is characterized by: $\tau_p = 2 \times 10^{-12}$ s (with $\alpha_m = 60$ cm^{-1} and $\alpha_i = 5$ cm^{-1}), $\eta_d = 80\%$, and $V_p = 5$ μm × 0.25 μm × 200 μm. The 20 log $[P_{ac}(\omega)/P_{ac}(0)]$ is used because photodetection generates an electrical *current* in direct proportion to the optical *power*. Thus, for a power ratio in the electrical circuit, this current must be squared.

of output powers. Note that the resonance is damped at low and high output powers. This occurs because the imaginary damping term in Eq. (2.54) depends on both ω_R and $1/\omega_R$. In Chapter 5, we will find that inclusion of gain compression and transport effects creates significantly more damping than predicted here. In fact, on real laser devices the resonance is typically limited to 5–10 dB (as opposed to the peak ~25 dB suggested in Fig. 2.13).

Beyond the strong resonance, the transfer characteristics degrade significantly. Thus, effective modulation of the output power can only be achieved over a modulation bandwidth of $\sim\omega_R$. When the damping is small, the electrical 3 dB down frequency (i.e., the frequency that reduces the received *electrical* power to one-half its DC value) is given by $\omega_{3\text{ dB}} = \sqrt{1+\sqrt{2}}\omega_R$. Expanding Eq. (2.53) using Eqs. (2.28), (2.38), and (2.40), we can express this result in terms of the output power:

$$f_{3\text{ dB}} \approx \frac{1.55}{2\pi}\left[\frac{\Gamma v_g a}{h\nu V}\frac{\eta_i}{\eta_d}\right]^{1/2}\sqrt{P_0}. \quad \text{(small damping)} \tag{2.55}$$

The modulation bandwidth of the laser can be steadily enhanced by increasing the output power. However, increased damping of the resonance at high powers, thermal limitations, and high power mirror facet damage set practical limits on the maximum average operating power we can use.

Because thermal limits are usually associated with the drive current, it is also convenient to express ω_R in terms of current. Using Eq. (2.37) for N_{p0}, with g_{th}

given by Eq. (2.28), Eq. (2.53) becomes

$$\omega_R = \left[\frac{\Gamma v_g a}{qV}\eta_i(I - I_{th})\right]^{1/2}. \qquad (2.56)$$

In this form we observe that it is desirable to enhance the differential gain, minimize the volume of the mode ($\Gamma/V = 1/V_p$), and maximize the current relative to threshold for maximum bandwidth. If we want to keep the overall drive current low, then we should also try to minimize the threshold current, perhaps by increasing the facet reflectivity. If, however, we are more concerned about keeping the photon density low (for example, to reduce the risk of facet damage), then from Eq. (2.52) we should try to decrease the cavity lifetime instead, perhaps by *decreasing* the facet reflectivity. Thus, the optimum cavity design for a high-speed laser depends on what constraints we place on the device operation. In Chapter 5 we will find that at very high powers, the maximum bandwidth actually becomes independent of ω_R and is more fundamentally related to the damping factor (the K-factor), which is affected by gain compression and transport effects.

Example 2.3 A cleaved facet, active 3-μm-wide and 500-μm-long ridge laser is created from the laser structure from Example 2.1. This ridge laser is biased 30 mA above threshold and directly modulated by applying a small signal sine wave current to its active section.

Problem: Determine the resonance peak frequency $f_R = \frac{\omega_R}{2\pi}$ of this laser, assuming injection efficiency η_i of 80%, and assuming no change in the internal losses.

Solution: To calculate the resonance frequency, we will use the Eq. (2.56). Therefore, we need to compute the differential gain a at threshold, since the carrier density is clamped at the threshold carrier density. Thus, we first need to determine the threshold carrier density. Because the internal losses and the laser length are unchanged, the threshold modal gain for this laser is the same as that for the laser in Example 2.2, $\Gamma g_{th} = 37.79\ \text{cm}^{-1}$, leading to the same threshold carrier density as calculated in Example 2.2,

$$N_{th} = N_{tr} e^{\frac{g_{th}}{g_{0N}}} = N_{tr} e^{\frac{37.79}{0.04 \cdot 1207.29}} = 2.6865 \cdot 10^{18}\ \text{cm}^{-3}.$$

Differential gain a can be computed using expression Eq. (2.46),

$$a = \frac{\partial g}{\partial N}\Big|_{N=N_{th}} = \frac{g_{0N}}{N_{th}} = \frac{1207.29\ \text{cm}^{-1}}{2.6865 \cdot 10^{18}\ \text{cm}^{-3}} = 4.49 \cdot 10^{-16}\ \text{cm}^2.$$

The resonance frequency is given by $f_R = \frac{\omega_R}{2\pi}$, where ω_R is defined in Eq. (2.56),

$$f_R = \frac{1}{2\pi}\left[\frac{\Gamma v_g a}{qV}\eta_i(I - I_{th})\right]^{1/2} = \left[\frac{\Gamma_1 v_g a}{qV_1}\eta_i(I - I_{th})\right]^{1/2}.$$

V_1 is the volume of a single quantum well, $V_1 = 3 \cdot 500 \cdot 0.003 \cdot 10^{-12}$ cm^3 = $4.5 \cdot 10^{-12}$ cm^3, and the group velocity for InGaAsP laser is $v_g = \frac{c}{3.8} = 0.7894 \cdot 10^{10}$ cm/s. Therefore, the resonance frequency is

$$f_R = \frac{1}{2\pi}\left[\frac{0.01 \cdot 0.7894 \cdot 10^{10} \cdot 4.49 \cdot 10^{-16}\ \text{cm}^2}{1.6 \cdot 10^{-19} \cdot 4.5 \cdot 10^{-12}} 0.8(0.3)\frac{1}{s^2}\right]^{1/2} = 5.47\ \text{GHz}.$$

To gain a somewhat more intuitive understanding of the natural resonant behavior that results between the carrier-photon coupling described by the coupled rate equations, we consider only the third term on the right side of Eq. (2.50), for the small-signal carrier density, N_1, together with Eq. (2.51) for the small-signal photon density, N_{p1}. This is approximately valid, because the carrier density is almost clamped, $N_{p1} \gg N_1$, so the other terms in Eq. (2.50) are much smaller. If we view the left-hand sides of these two equations as time derivatives, then we observe from Eq. (2.51) that as N_1 increases and becomes positive, N_{p1} increases in time due to increased gain in the laser. However, from the third term in Eq. (2.50), once N_{p1} becomes positive, it serves to decrease N_1 through increased stimulated emission. As N_1 decreases and becomes negative, N_{p1} begins to fall, and once it becomes negative, it again produces an increase in N_1. At this point, the cycle repeats itself. This phenomenon produces a natural resonance in the laser cavity which shows up as a ringing in the output power of the laser in response to sudden changes in the input current. The natural frequency of oscillation associated with this mutual dependence between N_1 and N_{p1} can be found by multiplying Eqs. (2.50) and (2.51) together, again ignoring all but the third term on the right-hand side of the first equation, we again obtain ω_R, given by Eq. (2.55), and commonly referred to as the *relaxation resonance frequency* (where *relaxation* refers to an attempt by the photons and carriers to relax to their steady-state values). It is directly proportional to the square root of the differential gain and average photon density in the cavity (output power) and inversely proportional to the square root of the photon lifetime in the cavity. The relaxation resonance of the laser cavity is much like the natural oscillation of an *LC* circuit. However, the additional terms present in Eq. (2.50) lead to more of an *RLC* circuit behavior, dampening the resonant response.

2.8 CHARACTERIZING REAL DIODE LASERS

In this section we wish to review some of the common measurements that are made on diode lasers. We shall emphasize those that can be used to extract internal parameters that we have used in the rest of this chapter. More complex characterization techniques will be delayed until after the discussion of dynamic effects and the introduction of more complex cavity geometries.

2.8.1 Internal Parameters for In-Plane Lasers: $\langle\alpha_i\rangle$, η_i, and g versus J

Perhaps the most fundamental characteristic of a diode laser is the P–I characteristic as has been illustrated in Fig. 2.9. From a measured P–I characteristic one can immediately determine the experimental threshold current, I_{th}, from the intercept of the above-threshold curve with the abscissa. The differential quantum efficiency, η_d, can be calculated from Eq. (2.41), provided the wavelength is known. Usually the mean mirror reflectivity, $R = r_1 r_2$, can be calculated with good accuracy, and the length, L, can be measured. Thus, the mirror loss, $\alpha_m \equiv (1/L)\ln(1/R)$ can be calculated. However, the net internal optical loss $\langle\alpha_i\rangle$ and quantum efficiency, η_i, cannot be determined from a single device.

To determine these important internal parameters, one commonly uses two or more lasers of different length fabricated from the same material with identical mirrors. This is relatively straightforward for in-plane lasers because the length can be varied at the final cleaving step. From Eq. (2.40) it can be seen that by measuring the differential efficiency of two such lasers, one is left with two equations containing two unknowns, $\langle\alpha_i\rangle$ and η_i. That is,

$$\eta_d = \frac{\eta_i \ln\left(\frac{1}{R}\right)}{L\langle\alpha_i\rangle + \ln\left(\frac{1}{R}\right)},$$

and

$$\eta_d' = \frac{\eta_i \ln\left(\frac{1}{R}\right)}{L'\langle\alpha_i\rangle + \ln\left(\frac{1}{R}\right)}, \qquad 2.63 \quad (2.57)$$

where L and L' are the lengths of the two different lasers. Solving, we find

$$\langle\alpha_i\rangle = \frac{\eta_d' - \eta_d}{L\eta_d - L'\eta_d'} \ln\left(\frac{1}{R}\right),$$

and

$$\eta_i = \eta_d \eta_d' \frac{L - L'}{L\eta_d - L'\eta_d'}. \qquad 2.64 \quad (2.58)$$

If indeed one can make two identical lasers except for their lengths, then Eqs. (2.58) will give the desired internal parameters. However, experimental data usually have some uncertainty which limits the utility of these expressions. For more reliability, it is generally better to plot a number of data points on a graph and determine the unknowns by fitting a curve to the data. In the present case it is most convenient to plot the reciprocal of the measured differential efficiencies versus L. Then a straight line through the data has a slope and intercept from which $\langle\alpha_i\rangle$ and η_i can be determined. More specifically,

$$\frac{1}{\eta_d} = \frac{\langle\alpha_i\rangle}{\eta_i \ln(1/R)} L + \frac{1}{\eta_i}. \qquad 2.65 \quad (2.59)$$

Thus, the intercept gives η_i, and this can be used in the slope to get $\langle\alpha_i\rangle$.

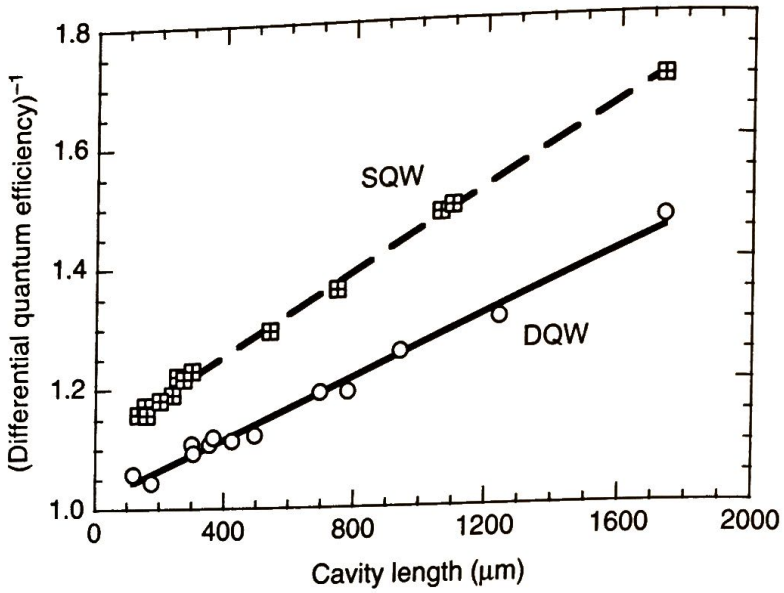

FIGURE 2.14: Plot of experimental reciprocal external differential efficiencies versus laser cavity length for 50 μm wide $In_{0.2}Ga_{0.8}As$ GRINSCH quantum well lasers. For both single-quantum-well (SQW) and double-quantum-well (DQW) cases, the $In_{0.2}Ga_{0.8}As$ well(s) was 80 Å wide. For the DQW a 12 nm GaAs separation barrier was used, and in both cases 40 nm of GaAs was used on each side of the well(s). On each side of this active region, the barrier stepped to $Al_{0.2}Ga_{0.8}As$ for 8 nm and then tapered to $Al_{0.8}Ga_{0.2}As$ over 80 nm to form the graded-index GRINSCH structure [1]. From these data the SQW had $\alpha_i = 3.2$ cm^{-1} and $\eta_i = 89.6\%$; and the DQW had $\alpha_i = 2.6$ cm^{-1} and $\eta_i = 98.6\%$.

Figure 2.14 shows such a plot for some data taken from broad-area in-plane InGaAs/GaAs quantum-well lasers. Single (SQW) and double (DQW) quantum-well cases are included [1].

For shorter cavity lengths, the data in Fig. 2.14 will fall above the line indicated. This data was ignored when determining the line fit because it represents a region where higher-order effects result in an incomplete clamping of the carrier density above threshold. The result is an apparent decrease in η_i (see Appendix 2 for details). If one assumes that the net internal loss does not change in this process, it is possible to estimate the decrease in η_i by repeated use of Eq. (2.59) or 2.35 for this high-gain points.

In the process of taking data, one can also generate a table of threshold current densities in the active region, $J_{th} = (\eta_i I_{th}/wL)$ versus L. These are usually taken from broad-area devices so that lateral current and carrier leakage can be neglected. From Eq. (2.25) we also see that corresponding threshold modal gains Γg_{th} can be calculated for each length once the internal loss is found. Thus, it is possible to construct the modal gain versus current density characteristic for the laser from these threshold values. This characteristic can usually be fitted well to an exponential, two parameter (J_{tr} and g_0) curve,

$$J = J_{tr} e^{\frac{g}{g_0}}. \tag{2.60}$$

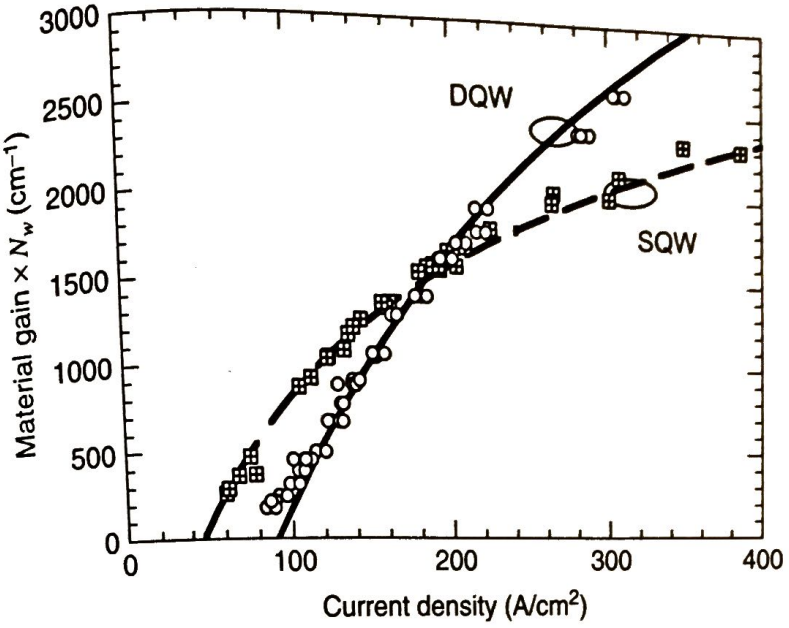

FIGURE 2.15: Experimentally determined gain versus current density for an InGaAs/GaAs quantum well laser described in Fig. 2.14 [1]. For the ordinate the modal gain Γg is divided by the confinement factor for one well Γ_w to give the material gain g times the number of wells, N_w. The solid curves are from a calculation based on the theory to be developed in Chapter 4.

Because the confinement factor, Γ, can usually be calculated as discussed in Appendix 5, one can ultimately determine the basic material gain versus current density characteristic for the active material. Figure 2.15 gives the result for the example in Fig. 2.14.

Example 2.4 To characterize the active material from Example 2.1, a 50-μm-wide and 500-μm-long broad area laser is cleaved from the wafer. Its pulsed threshold current is 47.94 mA and differential efficiency from both facets 48.24%. This laser is then re-cleaved into two 250-μm-long lasers, having pulsed threshold currents of 59.44 mA and differential efficiencies of 60.19%.

Problem: (1) What is the injection efficiency η_i? (2) What is the average internal modal loss? (3) Determine J_{tr} and g_0 in the gain vs current density characteristic for each quantum well, assuming $J = J_{tr} e^{\frac{g}{g_0}}$.

Solution: To calculate the injection efficiency η_i and the internal modal loss $\langle \alpha_i \rangle$, we will use the Eq. (2.58). Once the modal loss is known, and knowing the threshold current densities in the active region, we can construct the modal gain Γg versus current J density curve. Because the confinement factor is known, we can determine the basic material gain g versus current density J characteristic for this active material using the Eq. (2.60). From Eq. (2.58),

$$\langle \alpha_i \rangle = \frac{\eta_d' - \eta_d}{L\eta_d - L'\eta_d'} \ln\left(\frac{1}{R}\right) = \frac{(0.6019 - 0.4824)\ln\left(\frac{1}{0.32}\right)}{0.05 \cdot 0.4824 - 0.025 \cdot 0.6019} = 15 \text{ cm}^{-1}$$

and

$$\eta_i = \eta_d \eta_d' \frac{L - L'}{L\eta_d - L'\eta_d'} = 0.6019 \cdot 0.4824 \frac{0.025 \text{ cm}^{-1}}{0.0091} = 0.80.$$

For the gain versus current density characteristic, we utilize two data points from two different laser lengths:

$$J_{th1} = \frac{\eta_i I_{th1}}{w \cdot L_1} = \frac{0.8 \cdot 47.94 \text{ mA}}{500 \cdot 50 \cdot 10^{-8} \text{ cm}^2} = 153.41 \text{ A/cm}^2$$

$$J_{th2} = \frac{\eta_i I_{th2}}{w \cdot L_2} = \frac{0.8 \cdot 59.44 \text{ mA}}{250 \cdot 50 \cdot 10^{-8} \text{ cm}^2} = 380.42 \text{ A/cm}^2.$$

Threshold modal gain Γg_{th1} for the 500-μm cavity was calculated in Example 2.2 to be 37.79 cm^{-1}. Similarly, for the 250-μm-long cavity, the threshold modal gain is $\Gamma g_{th1} = 60.58 \text{ cm}^{-1}$, where $\Gamma = 0.04$, as discussed in Example 2.2. Finally,

$$g_0 = \frac{g_{th1} - g_{th2}}{ln \frac{J_{th1}}{J_{th2}}} = \frac{944.71 - 1514.43 \text{ cm}^{-1}}{ln \frac{153.41}{380.42}} = 627 \text{ cm}^{-1}$$

$$J_{tr} = \frac{J_{th1}}{\exp \frac{g_{th1}}{g_0}} = \frac{153.41 \text{ A/cm}^2}{\exp \frac{944.71}{627}} = 34 \text{ A/cm}^2.$$

2.8.2 Internal Parameters for VCSELs: η_i and g versus J, $\langle \alpha_i \rangle$, and α_m

In vertical-cavity lasers the preceding procedure is a little difficult to carry out because the cavity length is set by the crystal growth. Multiple growths may result in other changes in the material besides the cavity length. Therefore, it has been proposed that the desired information can be determined by making in-plane cleaved lasers fabricated from the vertical-cavity laser material. However, a somewhat different approach is followed. Clearly, the internal loss determined for the in-plane laser will not be the same as for the VCSEL because the optical mode travels through a different cross section of materials. Nevertheless, if the electrical pumping current follows the same path and the threshold current densities covered in the in-plane diagnostic lasers includes the VCSEL values, the measured internal quantum efficiency should be the same.

The most valuable piece of information provided by the diagnostic lasers is the gain versus current density characteristic. Combining this characteristic and the internal quantum efficiency from the in-plane lasers together with the measured threshold current density and differential quantum efficiency from the VCSEL, we now have enough information to unambiguously determine the VCSEL internal loss and mirror loss (and thus, reflectivity). That is, Eqs. (2.40) and (2.25) can be solved for $\langle \alpha_i \rangle$ and α_m because Γg_{th}, η_d, and η_i are known. The results are

$$\alpha_m = \Gamma g_{th} \frac{\eta_d}{\eta_i} \qquad (2.61)$$

and

$$\langle \alpha_i \rangle = \Gamma g_{th} \left[1 - \frac{\eta_d}{\eta_i} \right] \qquad 2.68 \ (2.62)$$

As before, the confinement factors for both the in-plane diagnostic lasers and the VCSELs must be calculated.

2.8.3 Efficiency and Heat Flow

Just as the differential efficiency is important in determining the electrical to optical modulation efficiency, the overall net power conversion efficiency is also important in determining the achievable optical power out as well as the circuit heating and system power requirements. This so-called wall-plug efficiency is simply the optical power out relative to the electrical power in, $\eta = P_0/P_{in}$. The optical power out is given by Eq. (2.39), and the electrical power in is the product of the drive current and the total voltage across the diode's terminals. We can express this as

$$P_{in} = I^2 R_s + I V_d + I V_s, \qquad 2.69 \ (2.63)$$

where R_s is the series resistance, V_s is a current-independent series voltage, and V_d is the ideal diode voltage, which is equal to the quasi-Fermi level separation. This voltage is clamped at its threshold value above threshold.

The power dissipated in the laser is

$$P_D = P_{in} - P_0 = P_{in}[1 - \eta], \qquad 2.70 \ (2.64)$$

and the temperature rise is

$$\Delta T = P_D Z_T, \qquad 2.71 \ (2.65)$$

where Z_T is the thermal impedance. Analytic expressions for Z_T, which are approximately valid for several practical cases of interest, exist. Three are illustrated in Fig. 2.16. For a heat sink plane positioned much closer than the lateral dimensions

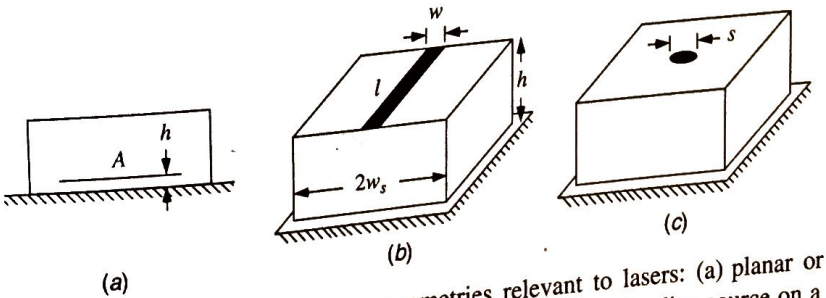

FIGURE 2.16: Schematics of heat flow geometries relevant to lasers: (a) planar or one-dimensional flow for a heat sink relatively near the heat source, (b) a line source on a thick substrate, and (c) a disk source on a half-space.

of the regions generating the heat (Fig. 2.16a), a one-dimensional heat flow can be assumed. In this case,

$$Z_T = \frac{h}{\xi A}, \quad \text{(1-D flow)} \tag{2.72 (2.66)}$$

where ξ is the thermal conductivity of the material separating the source of area A a distance h from the ideal sink. For GaAs and AlAs, $\xi \sim 0.45$ and 0.9 W/cm-°C. For $Al_xGa_{1-x}As$, alloy scattering reduces ξ to a minimum of 0.11 W/cm-°C at $x \approx 0.5$. For InP and InGaAsP, the values are $\xi \sim 0.68$ and 0.06 W/cm-°C.

For a linear stripe heat source of length l and width w on a thick substrate (thickness h), which is somewhat wider (width $2\,w_s$) than this thickness (Fig. 2.16b), a quasi two-dimensional heat flow results. Then,

$$Z_T \approx \frac{\ln(4h/w)}{\pi \xi l}. \quad \text{(line : } w \ll h < w_s\text{)} \tag{2.73 (2.67)}$$

A narrow stripe in-plane laser mounted active region up on a relatively thick substrate approximates this case. For a disk heat source of diameter s on a half-space (Fig. 2.16c), a three-dimensional flow into the half-space can be assumed. Then,

$$Z_T = \frac{1}{2\xi s}. \quad \text{(small disk)} \tag{2.74 (2.68)}$$

This is approximately valid for a small-diameter VCSEL mounted on the top side of a relatively thick substrate.

2.8.4 Temperature Dependence of Drive Current

The required drive current for a given power out of a laser is given by Eq. (2.50), in which the first and second terms give the needed current above threshold and the threshold current, respectively. In this equation it is assumed that the recombination below threshold is dominated by spontaneous emission events. If significant nonradiative recombination exists, an additional threshold term, such as Eq. (2.52), must be added. For both in-plane and vertical cavity lasers these expressions are functions of temperature. Generally, more current is required both for threshold and the increment above threshold as the temperature is increased, and we can estimate the nature of this dependence by exploring the temperature dependence of each of the factors in the terms of Eqs. (2.50) and (2.52).

However, for VCSELs as well as single axial-mode in-plane lasers, the situation is complicated by the integrated mode selection filter (e.g., Bragg mirrors), which can force the lasing mode to be well off the wavelength where the gain is a maximum. Thus, such lasers can be designed to have anomolous temperature behavior because the wavelength of the cavity mode and the gain peak shift at different rates versus temperature. In fact, by deliberately misaligning the mode

from the gain peak at room temperature, it is even possible to make the threshold go down with increasing temperature as the gain moves into alignment with the mode [4]. In this section, we will not consider these relative mode–gain alignment issues. Rather, we will assume that a spectrum of modes exist, as in a simple in-plane laser, so that lasing always can occur at the gain peak. Thus, we again can focus only on the temperature dependence of the various factors in Eqs. (2.50) and (2.52).

For the threshold current in Eq. (2.49), three factors generally have a significant temperature dependence: N_{tr}, g_0, and $\langle \alpha_i \rangle$. From the gain calculations of Chapter 4, it may be shown that over some range of temperatures, $N_{tr} \propto T$, $g_0 \propto 1/T$, and $\langle \alpha_i \rangle \propto T$. The transparency carrier density is increased and the gain parameter is reduced because injected carriers spread over a wider range in energy with higher temperatures. The increased internal loss results from the required higher carrier densities for threshold. From Eq. (2.49), we conclude that both the gain and the internal loss variations result in an exponential temperature dependence of the threshold current, whereas the linear dependence of the transparency carrier density is not significant over small temperature ranges. Additional threshold components such as Eq. (2.52) will introduce further temperature dependencies. For example, in Chapter 4 and Appendix 2 it is shown that $C \propto \exp(\gamma_C T)$ and $R_l \propto \exp(\gamma_l T)$. Thus, Auger recombination and carrier leakage both contribute additional exponential increases in the threshold current. These observations suggest that the threshold current can be approximately modeled by

$$I_{th} = I_0 e^{T/T_0}, \qquad (2.69)$$

where T_0 is some overall characteristic temperature, and both temperatures are given in degrees Kelvin, K. Note that small values of T_0 indicate a larger dependence on temperature (since $dI_{th}/dT = I_{th}/T_0$). It should also be noted that any minor temperature dependence of other parameters can easily fit into this model over some limited temperature range. For example, the internal efficiency can decrease at higher temperatures due to increased leakage currents and/or higher-order effects discussed in Appendix 2. This decrease in η_i will show up as a reduction of T_0 over a limited temperature range, regardless of the exact dependence of η_i on temperature.

For good near-infrared (~850 nm) GaAs/AlGaAs DH lasers, observed values of T_0 tend to be greater than 120 K near room temperature. For quantum-well GaAs/AlGaAs the values are somewhat higher (~150 – 180 K), and for strained-layer InGaAs/AlGaAs quantum wells, $T_0 \geq 200$ K have been observed. For 1.3 – 1.55 μm InGaAsP/InP DH and quantum-well lasers the characteristic temperature is generally quite a bit lower as expected. Measured values tend to fall in the 50–70 K range, due to Auger recombination as well as possible carrier leakage and intervalence band absorption effects. Thus, the threshold tends to change significantly between room temperature and 100°C, usually resulting in relatively poor performance at the higher temperatures, and generally requiring the use of thermoelectric coolers. Shorter wavelength (600–800 nm) AlGaAs/GaAs

and AlInGaP/GaAs lasers also tend to have a smaller T_0 than the near-infrared variety, presumably due to increased carrier leakage.

The above-threshold current required to obtain a desired output power is also temperature dependent, although the dependence is usually smaller than for the threshold current. This dependence results from a reduction in the differential quantum efficiency. As suggested by the constituent factors in the first term in Eq. (2.50), an increase in $\langle \alpha_i \rangle$ as well as a drop in η_i are usually the cause of the increase in $I - I_{th}$. In analogy with Eq. (~~2.69~~), we can write

$$I - I_{th} = I_{p0} e^{T/T_\eta}, \qquad (~~2.70~~)$$

where T_η is the characteristic temperature for the above-threshold current increment. T_η is generally two or three times larger than T_0, as might be expected from the above discussion. That is, T_0 includes several effects in addition to those in T_η.

In practice one is typically more interested in the relative changes in threshold current and differential efficiency as the temperature varies rather than the absolute values as given in Eqs (~~2.69~~) and (~~2.70~~), so more useful expressions tend to be the ratios of currents and differential efficiencies at two different temperatures, T_1 and T_2:

$$\frac{I_{th1}}{I_{th2}} = e^{(T_1 - T_2)/T_0} \qquad (~~2.71~~)$$

$$\frac{\eta_{d1}}{\eta_{d2}} = e^{-(T_1 - T_2)/T_\eta}. \qquad (~~2.72~~)$$

Example 2.5 Another batch of lasers similar to those from Example 2.3 is made, but this time, the laser contacts exhibit large series resistance, and thus lead to significant amount of heating under CW operation. Consider a 250-μm-long, 3-μm-wide all-active ridge laser, which can be modeled by a 50 Ω series resistance and an ideal diode with voltage $V_d = 0.88$V. The InP substrate is 100 μm thick and 500 μm wide, and it is bonded to a good heat sink. The characteristic temperature for threshold current is $T_0 = 25$ K and that for differential efficiency is $T_\eta = 110$ K. Pulsed threshold current is 15 mA, and differential efficiency out of both ends 48.24%.

Problem: (1) What is the thermal impedance (2) What is the new CW threshold current (3) At a bias of 50 mA, what is the power out and the temperature rise of the active region?

Solution: Thermal impedance can be calculated using Eq. (2.67),

$$Z_T = \frac{\ln(4h/w)}{\pi \xi l} = \frac{\ln \frac{4 \cdot 100}{3}}{\pi \cdot 0.6 \cdot 250 \cdot 10^{-4}} = 103.78^\circ \text{ C/W}$$

To find the new threshold current, we will need to iterate, given that the temperature increase depends on the new threshold current, which in turn is determined by

the temperature increase. At threshold, the output power from the laser can be neglected; therefore, the dissipated power is equal to the input power,

$$P_D = P_{in} = I_{th}^2 \cdot R_s + I \cdot V_d,$$

where V_d is the ideal diode voltage and is approximately 0.88 V for InGaAsP/InP. Assuming that the threshold current increase due to heating is 1 mA, $I_{th} = 16$ mA, the dissipated power and temperature increase are

$$P_D = (0.016)^2 \cdot 50 + (0.016)(0.88) \text{ mW} = 26.88 \text{ mW}$$
$$\Delta T = P_d Z_T = 0.02688 \cdot 103.78^\circ\text{C} = 2.79^\circ\text{C}.$$

To check, we plug in the value for ΔT to calculate the threshold current based on known $T_0 = 25$ K,

$$I'_{th}(\Delta T = 2.79^\circ\text{C}) = 15 \text{ mA} \cdot \exp\frac{2.79}{25} = 16.77 \text{ mA}.$$

Thus, we conclude that we have underestimated the heating effects, and we use I'_{th} to calculate the dissipated power and repeat the process. After a couple of iterations, we end up with the final value for I_{th},

$$I_{th} = 16.9 \text{ mA}.$$

To calculate the output power for the bias current of $I = 50$ mA, we do the following: assuming that the output power is negligible, we calculate the dissipated power, the temperature increase, and then the increase in the threshold temperature and the decrease in the differential efficiency. At that point, we can compute the output power. To iterate, we reduce the dissipated power by the output power value and repeat the process. After a couple of steps, the process converges.

$$P_D \cong P_{in} = (0.05)^2 \cdot 50 + (0.05)(0.88) \text{ mW} = 169.00 \text{ mW}$$
$$\Delta T = P_D Z_T = 0.169 \cdot 103.78^\circ\text{C} = 17.54^\circ\text{C}$$

The threshold current and the differential efficiency with this much temperature increase are given by

$$I'_{th} = 15 \text{ mA} \cdot \exp\frac{17.54}{25} = 30.25 \text{ mA}$$
$$\eta'_d = 0.4824 \cdot \exp\frac{-17.54}{110} = 0.4113.$$

The output power is given by

$$P_o = \frac{h\nu}{q}\eta'_d(I - I_{th}') = 0.8 \cdot 0.4113(50 - 30.25) \text{ mW} = 6.49 \text{ mW}.$$

Reducing the dissipated power by P_o yields $\Delta T = 16.87°C$ and $P_o = 6.80$ mW. Repeating the process yields the final values of

$$\Delta T = 16.83°C$$

$$P_o = 6.82 \text{ mW}.$$

The L-I characteristic of this laser is illustrated in Fig. 2.17.

2.8.5 Derivative Analysis

Real diode lasers do not always have perfectly linear $P-I$ characteristics above threshold, and they have parasitic series resistance as well as a possible series voltage as outlined in Eq. (2.63) above. Derivatives of the $P-I$ and $V-I$ characteristics can be useful in sorting out these nonidealities. The dP/dI characteristic in an ideal laser would only provide a good measure of the threshold current and a slope to determine η_d above threshold. However, actual $P-I$ characteristics can have kinks, and they tend to be nonlinear. The kinks can indicate a switching between lateral or axial modes or an additional parasitic mirror in the device. These are obviously emphasized in a derivative curve. Premature saturation of the output power may indicate the existence of current leakage paths that "turn-on" at higher current levels or excessive heating of the gain material. The derivative curve gives a good quantitative measure of these symptoms. Figure 2.18(a) gives example plots of $P-I$ and dP/dI for an in-plane laser.

In addition to the $V-I$ characteristic, it is common to plot IdV/dI versus I. This latter characteristic gives a sensitive measure of the series resistance, and it

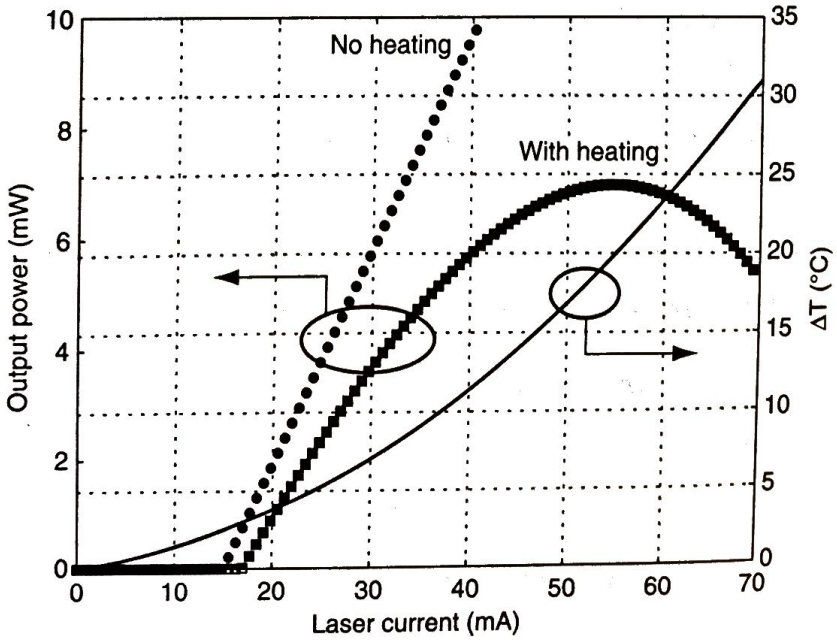

FIGURE 2.17: Illustration of Example 2.5—laser heating as a function of bias current, L-I curve with thermal roll off (temperature effects taken into account) and ideal L-I curve (for no heating) are shown.

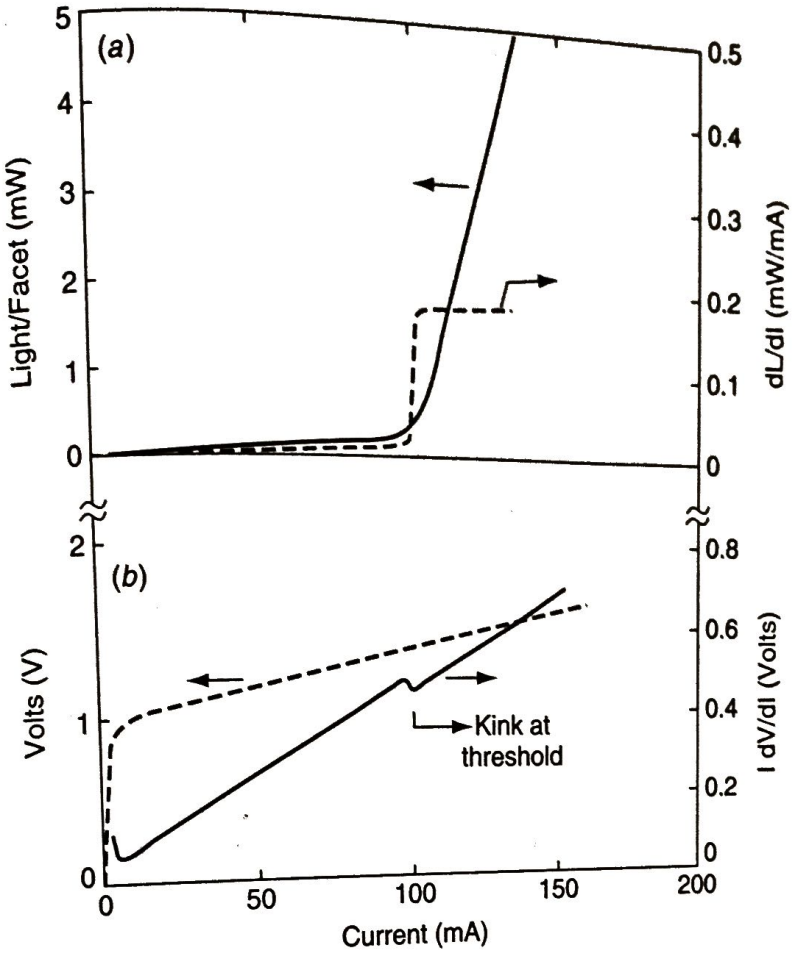

FIGURE 2.18: (a) Plots of optical output power, P, and its derivative, $dP/dI \equiv dL/dI$, versus drive current, I, for a stripe-geometry gain-guided InGaAsP laser. (b) Plots of the terminal voltage, V, and IdV/dI versus current for the same device [5]. (*Reproduced, by permission, from Semiconductor Lasers.*)

is particularly useful in identifying shunt current paths. Because the voltage across the junction clamps at threshold with the carrier density, a kink in the curve occurs at that point. Figure 2.18b shows example plots of both V and IdV/dI versus I. The information contained in the plot can be derived by considering an equivalent circuit with a parasitic resistance in series with an ideal heterojunction diode. The diode $V - I$ is described by

$$I = I_0[e^{qV_d/nkT} - 1]. \tag{2.73}$$

Taking the derivative of the terminal voltage, $V = V_d + IR$, and solving for dV_d/dI from Eq. (2.73), we obtain for $I \gg I_0$ but below threshold,

$$I\frac{dV}{dI} = \frac{nkT}{q} + IR. \tag{2.74}$$

Above-threshold V_d is constant, so

$$I\frac{dV}{dI} = IR. \tag{2.75}$$

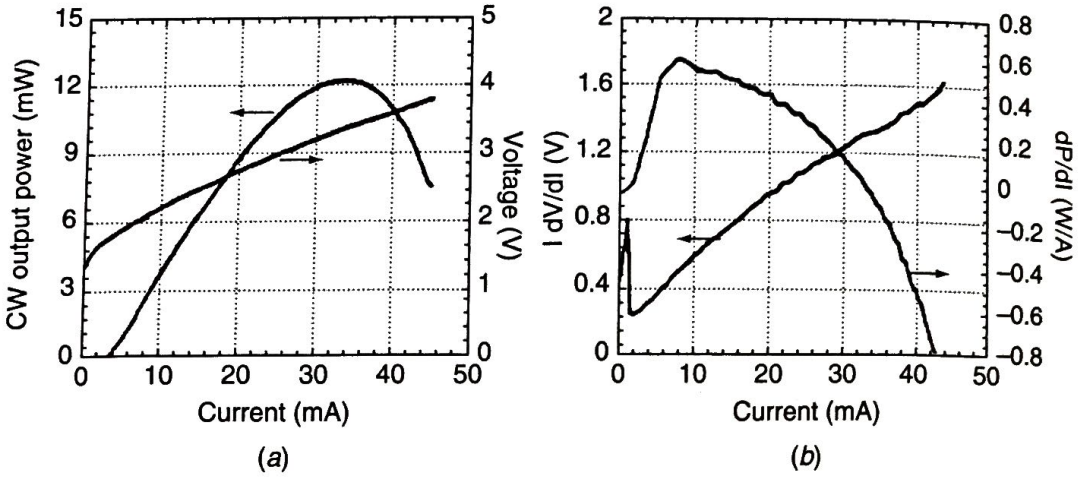

FIGURE 2.19: (a) Output power and terminal voltage for a 20 μm diameter VCSEL with three InGaAs strained quantum wells and AlAs/GaAs DBR mirrors. (b) Derivative curves for the same device [6].

Thus, we see that the slope above and below threshold should be R, but there is a positive offset of nkT/q below threshold, which provides a kink of this magnitude at threshold. Now if a shunt resistance is added to the equivalent circuit, it turns out that an additional term must be added to Eq. (2.74). This provides a peak in the $I(dV/dI)$ characteristic below threshold. For common DH structures the diode ideality factor $n \sim 2$.

Figure 2.19 gives plots analogous to Fig. 2.18 for an InGaAs/GaAs VCSEL. Here, significant local heating causes the $P-I$ curve to roll over at relatively low powers. This results in a negative dP/dI beyond this point. In addition, significant series resistance makes it difficult to discern the nkT/q kink in the IdV/dI characteristic at threshold. Thus, the derivative analysis is not always very effective for VCSELs.

REFERENCES

1. Hu SY, Young DB, Corzine SW, Gossary AC, Coldren LA. High-efficiency and low-threshold InGaAs/AlGaAs quantum-well lasers. *J Appl Phys* 1994;**76**: 3932–3934.
2. Krames MR, Shchekin OB, Mueller-Mach R, Mueller GO, Ling Zhou, Harbers G, Craford MG, Philips Lumileds Lighting Co. Status and future of high-power light-emitting diodes for solid-state lighting. *J Display Tech* 2007;**3**(2): 160–175.
3. Oder TN, Kim KH, Lin JY, Jiang HX. III-nitride blue and untraviolet photonic crystal light emitting diodes. *Appl Phys. Lett.* 2004;**84**: 466.
4. Young DB, Scott JW, Peters FH, Peters MG, Majewski ML, Thibeault BJ, Corzine SW, Coldren LA. Enhanced performance of offset-gain high-barrier vertical-cavity surface-emitting lasers. *IEEE Journal of Quantum Electronics* 1993;**29**(6): 2013–2022.
5. Agrawal GP, Dutta NK. *Semiconductor lasers*. 2nd ed. New York: Van Nostrand Reinhold; 1993.
6. Peters MG. [dissertation]. Santa Barbara, CA: University of California, Santa Barbara; 1995.

READING LIST

Agrawal GP, Dutta NK. *Semiconductor lasers*. 2nd ed. New York: Van Nostrand Reinhold; 1993.

Ebeling KJ. *Integrated opto-electronics*. Berlin: Springer-Verlag; 1993.

Verdeyen JT. *Laser electronics*. 2nd ed. Upper Saddle River, NJ: Prentice Hall; 1989.

Yariv A. *Optical electronics*. 4th ed. Philadelphia: Saunders College Publishing; 1991.

PROBLEMS

These problems draw on material from Appendices 4 through 6.

1. In a diode laser, the terminal current is I, the current bypassing the active region is I_b, the current due to carriers leaking out of the active region before they recombine is I_l, the current contributing to nonradiative recombination in the active region is I_{nr}, the current contributing to spontaneous emission in the active region is I_{sp}, the currents contributing to spontaneous emission and nonradiative recombination outside the active region are I'_{sp} and I'_{nr}, respectively, and the current contributing to stimulated emission in the active region is I_{st}.
   (a) What is the injection efficiency?
   (b) If the measured external differential efficiency above threshold is η_d, what is the ratio of the mirror loss to the total cavity loss?
   (c) For below-threshold operation, what is the radiative efficiency?

2. A reservoir of area A is filled at a rate of R_f (in $\text{ft}^3/\text{min.}$) and simultaneously drained from two pipes that have flow rates that depend on the height of water, h. The drain rates are, $R_{d1} = C_1 h$ and $R_{d2} = C_2 h^2$, respectively.
   (a) Write a rate equation for the water height.
   (b) What is the steady-state water height?
   (c) If $A = 100\ \text{ft}^2$, $R_f = 10\ \text{ft}^3/\text{min}$, and $C_1 \approx 0$, what is C_2 for a steady-state depth of 5 ft?

3. What is the approximate intrinsic cutoff frequency of an LED with a p-type active region doping of $6.3 \times 10^{18}\ \text{cm}^{-3}$?

4. The relative increase in photons in passing through a piece of GaAs is found to be $[1/N_p][dN_p/dt] = 10^{13}\ \text{s}^{-1}$. What is the material gain in cm^{-1}?

5. A 1.3 μm wavelength InGaAsP/InP diode laser cavity is found to have an optical loss rate of $4 \times 10^{12}/\text{s}$.
   (a) What is the photon lifetime?
   (b) What is the threshold modal gain?

6. In a cleaved-facet 1.55 μm InGaAsP/InP multiple quantum-well laser 400 μm in length, it is known that the injection efficiency and losses are 80% and $10\ \text{cm}^{-1}$, respectively.

(a) What is the threshold modal gain?

(b) What is the differential efficiency?

(c) What is the axial mode spacing?

7. A cleaved-facet, DH GaAs laser has an active layer thickness of 0.1 μm, a length of 300 μm, and a threshold current density of 1 kA/cm^2. Assume unity injection efficiency, an internal loss of 10 cm^{-1}, a confinement factor of 0.1, and only radiative recombination.

(a) What is the threshold carrier density in the active region?

(b) What is the power out of one cleaved facet per micrometer of width at a current density of 2 kA/cm^2?

(c) What are the photon and carrier densities at 2 kA/cm^2?

8. In the device of Problem 2.7, gain transparency ($g = 0$) is found to occur at 0.5 kA/cm^2 and the transverse confinement factor is 0.15. What is the relaxation resonance frequency at 2 kA/cm^2?

9. Two broad-area DH 1.3 μm InGaAsP/InP lasers are cleaved from the same material. One is 200 μm long and the other is 400 μm long. The threshold current densities are found to be 3 kA/cm^2 and 2 kA/cm^2, respectively, and the differential efficiencies including both ends are measured to be 60% and 50%, respectively.

(a) What are the injection quantum efficiency and internal loss for this material?

(b) For a ±1% error in each of the measured differential efficiencies, what are the errors in the calculated internal loss and quantum efficiency?

10. For the material of Problem 2.9, the relaxation resonance frequency for the 200-μm laser biased at twice threshold is found to be 3 GHz. What is the resonance frequency for the 400-μm device also biased at twice threshold?

11. A VCSEL is formed with multilayer AlGaAs mirrors and a 3-quantum-well GaAs active region. Current is injected through the mirrors. At a terminal current density of 1 kA/cm^2 the active region provides 1% of one-pass gain for the propagating axial mode. The injection efficiency is assumed to be 80%, and the average internal loss is 25 cm^{-1}. The effective cavity length is 1.5 μm.

(a) What mean mirror reflectivity is necessary for the device to reach threshold at 1 kA/cm^2?

(b) For this case, plot the output power density versus terminal current density.

(c) If we assume the gain is linear with carrier density, and that only spontaneous recombination is important below threshold, plot the threshold current density versus mean mirror reflectivity for $0.98 < R < 1.0$. On the opposite axis label the differential efficiency at each 0.005 reflectivity increment.

12. With the VCSEL material of Problem 2.11, etched square mesas are now formed measuring s on each side. Assuming a spontaneous bandwidth of 30 nm, an axial confinement factor of 2 L_a/L, lateral confinement factors of unity, and that the approximations of Appendix 4 are valid, plot the spontaneous emission factor versus s.

13. Again with the VCSEL material of Problem 2.11, square mesas are formed measuring s on each side by etching down to the active region, as illustrated in Fig. 1.15. The GaAs substrate may be assumed to be thick and wide. If we assume a threshold current density of 1 kA/cm^2 independent of area, a series voltage of 1 V, and a series resistance that is inversely proportional to device area, $R_s = 20$ kΩ-μm^2/s^2.

(a) Plot the temperature at the base of the mesa (active region location) versus s for a current of twice threshold. Cover $1 < s < 20$ μm.

(b) Assuming a differential efficiency of 50%, plot the power out and required current versus s for the conditions of (a).

14. An MQW-SCH InGaAsP/InP laser wafer with emission wavelength near 1.55 μm has been grown and characterized with broad area chips. Alternate active and passive regions are included. The active region contains 6–7 nm thick unstrained quaternary quantum wells (with lowest conduction and valence band quantum state energies spaced by 0.8 eV) separated by 5–8 nm quaternary barriers (having photoluminescense emission at 1.3 μm), all centered within a 1.3 μm-Q SCH waveguide, which all measures 350 nm in total thickness; the passive region does not have quantum wells, but is all 1.3 μm-Q material, again 350 nm thick. We can neglect optical reflections between the active and passive waveguides. A calculation indicates that the transverse confinement factor in the active is $\Gamma = 0.08$. Measurements on three different broad-area, cleaved-facet chips show that the modal losses in the active and passive sections are 15 cm^{-1} and 5 cm^{-1}, respectively, and that the injection efficiency to the active is 70%. A material gain curve is also derived for the quantum wells. Fitting to an expression of the form $g = g_{0J} \ln(J/J_{tr})$, it is found that $g_{0J} = 600$ cm^{-1}, and $J_{tr} = 100$ A/cm^2 per well. It is also found that the recombination rate for nominal threshold gains is composed of a mix of radiative and Auger recombination, such that the carrier density varies approximately as $J^{0.4}$.

We create three cleaved facet, 3-μm-wide ridge lasers from this material (lateral current and carrier spreading as well as any additional scattering losses can be neglected): the first is an active–passive laser with active and passive sections each 500 μm long; the second is an all active laser 500 μm in length; the third is another all active laser 250 μm in length. Measured small-signal frequency response of the 500–500 μm active–passive laser gives a resonance peak at 5 GHz, for a bias current 30 mA above threshold. Neglecting heating effects:

(a) What are the differential efficiencies (considering the emission from both ends) of each of the three lasers?

(b) What are the threshold currents of each of the three lasers?

(c) What is the differential gain, dg/dN, for this laser above threshold?

(d) What is the approximate threshold carrier density?

(e) What is the transparency carrier density? (Assume a logarithmic g versus N dependence)

(f) What are the expected relaxation resonance frequencies for the 500-μm and 250-μm all-active devices at 30 mA above their threshold currents?

15. We now make another batch of similar lasers from the same material as in Problem 2.13, but this time we mess up the contacting procedure such that the lasers have a relatively large series resistance, and thus, a significant amount of heating under continuous wave operation. Consider the 250-μm-long, 3-μm-wide, all-active device, which can be modeled by a 50 Ω series resistance and an ideal diode with an ideality factor of 3. The InP substrate is 90 μm thick and 500 μm wide; it is bonded to a good heat sink. The characteristic temperature for threshold current is $T_0 = 55$ K, and the characteristic temperatur for differential efficiency is $T_\eta = 110$ K.

(a) What is the thermal impedance of this laser?

(b) What is the new CW threshold current?

(c) At a bias of 50 mA, what is the power out and the temperature rise at the active region?

(d) Plot the output power and temperature rise versus CW current up to 100 mA. Compare to the pulsed output power on the same plot.

16. In a 1.55 μm InGaAsP/InP BH laser, the active region is 0.2 μm thick, 3 μm wide and 300 μm long. The injection efficiency is 70%. In addition, there is a 400-μm-long passive waveguide channel with the same lateral and transverse dimensions butted to the end of the active region. The transverse and lateral confinement factors are 0.2 and 0.8, respectively. Cleaved mirrors form a 700-μm-long cavity, and other internal reflections can be neglected. The material losses are 80 cm^{-1}, 20 cm^{-1}, and 5 cm^{-1} in the active, passive, and cladding regions, respectively. The gain versus carrier density characteristic for the active material is linear with a transparency carrier density of 2×10^{18} cm^{-3} and a differential gain of 5×10^{-16} cm^2. Assume a spontaneous emission bandwidth of 100 nm. At transparency the Auger recombination rate equals the spontaneous recombination rate, and other nonradiative terms can be neglected.

(a) Plot the P–I characteristic, labeling the threshold current, the spontaneous emission power into the mode at threshold, and the differential efficiency above threshold.

(b) Plot the small-signal frequency response for a bias current of twice threshold.

17. Using Eq. (A6.25) calculate the gain 50 meV above the band edge in GaAs as a function of $(f_2 - f_1)$. (Assume $\tau_{sp}^{21} = 0.3$ ns, and consider only the heavy-hole band.)

(b) What are the threshold currents of each of the three lasers?

(c) What is the differential gain, dg/dN, for this laser above threshold?

(d) What is the approximate threshold carrier density?

(e) What is the transparency carrier density? (Assume a logarithmic g versus N dependence)

(f) What are the expected relaxation resonance frequencies for the 500-μm and 250-μm all-active devices at 30 mA above their threshold currents?

15. We now make another batch of similar lasers from the same material as in Problem 2.15, but this time we mess up the contacting procedure such that the lasers have a relatively large series resistance, and thus, a significant amount of heating under continuous wave operation. Consider the 250-μm-long, 3-μm-wide, all-active device, which can be modeled by a 50 Ω series resistance and an ideal diode with an ideality factor of 3. The InP substrate is 90 μm thick and 500 μm wide; it is bonded to a good heat sink. The characteristic temperature for threshold current is $T_0 = 55$ K, and the characteristic temperatur for differential efficiency is $T_\eta = 110$ K.

(a) What is the thermal impedance of this laser?

(b) What is the new CW threshold current?

(c) At a bias of 50 mA, what is the power out and the temperature rise at the active region?

(d) Plot the output power and temperature rise versus CW current up to 100 mA. Compare to the pulsed output power on the same plot.

16. In a 1.55 μm InGaAsP/InP BH laser, the active region is 0.2 μm thick, 3 μm wide and 300 μm long. The injection efficiency is 70%. In addition, there is a 400-μm-long passive waveguide channel with the same lateral and transverse dimensions butted to the end of the active region. The transverse and lateral confinement factors are 0.2 and 0.8, respectively. Cleaved mirrors form a 700-μm-long cavity, and other internal reflections can be neglected. The material losses are 80 cm^{-1}, 20 cm^{-1}, and 5 cm^{-1} in the active, passive, and cladding regions, respectively. The gain versus carrier density characteristic for the active material is linear with a transparency carrier density of 2×10^{18} cm^{-3} and a differential gain of 5×10^{-16} cm^2. Assume a spontaneous emission bandwidth of 100 nm. At transparency the Auger recombination rate equals the spontaneous recombination rate, and other nonradiative terms can be neglected.

(a) Plot the $P-I$ characteristic, labeling the threshold current, the spontaneous emission power into the mode at threshold, and the differential efficiency above threshold.

(b) Plot the small-signal frequency response for a bias current of twice threshold.

17. Using Eq. (A6.25) calculate the gain 50 meV above the band edge in GaAs as a function of $(f_2 - f_1)$. (Assume $\tau_{sp}^{21} = 0.3$ ns, and consider only the heavy-hole band.)

an effective length. However, because ϕ_{eff} explicitly depends on β_p, not β_a, we choose to define the effective length as

$$L_{eff} = -\frac{1}{2}\frac{d\phi_{eff}}{d\beta_p}. \tag{3.39}$$

The mode spacing can be defined in terms of wavelength, $d\beta_a = -d\lambda(2\pi/\lambda^2)\bar{n}_{ga}$; or in terms of frequency, $d\beta_a = d\nu(2\pi/c)\bar{n}_{ga}$, where $\bar{n}_g = \bar{n} - \lambda\partial\bar{n}/\partial\lambda$. Furthermore, it follows that $d\beta_p/d\beta_a = \bar{n}_{gp}/\bar{n}_{ga}$. Using these expressions in Eq. (3.38), the mode spacing in either wavelength or frequency becomes

$$d\lambda = \frac{\lambda^2}{2(\bar{n}_{ga}L_a + \bar{n}_{gp}L_{eff})} \quad \text{or} \quad d\nu = \frac{c}{2(\bar{n}_{ga}L_a + \bar{n}_{gp}L_{eff})}. \tag{3.40}$$

If no reflection exists at the active–passive interface ($r_2 = 0$) and r_3 is positive and real, then $\phi_{eff} = -2\beta_p L_p$, and $L_{eff} = L_p$, reducing Eq. (3.40) to Eq. (2.29) given earlier. For the more general Fabry–Perot etalon, the slope of the phase will be dependent on whether we are near a resonance or an antiresonance of the etalon (as shown earlier in Fig. 3.6). Thus, L_{eff} can be larger or smaller than L_p. However, if the phase varies rapidly and nonlinearly within the range of one mode spacing (for example, near the Fabry–Perot resonances ($\beta L = m\pi$) in Fig. 3.6), then Eq. (3.40) will most likely not be very accurate because this derivation assumes that ϕ_{eff} varies linearly over at least one mode spacing.

The differential quantum efficiency and power out of end 1 are given by Eqs. (3.32) and (3.33), respectively, using Eq. (3.31). The second mirror reflectivity, r_2, in these single-section laser expressions should be replaced by r_{eff} wherever it shows up, and the mirror loss, α_m, is given by the second term in Eq. (3.36).

Figure 3.6 gives plots of the magnitude of r_{eff} in the special case where $r_2 = -r_3$ and loss can be neglected. As can be seen, the magnitude of the reflectivity of this mirror can vary significantly, and this will provide a filtering effect on the cavity modes. As indicated by Eq. (3.36), the modes with the lowest loss or highest mirror reflectivity will tend to lase first. Thus, such a second section or etalon can be used to filter out unwanted modes. However, a point often confused is that the maxima of r_{eff} always occur at the antiresonances of the etalon. Thus, in the three-mirror configuration, having a high-Q external cavity actually leads to worse mode selectivity because the maxima become very flat in this case. In fact, there is an optimum value of net external cavity loss that provides the largest curvature at the maxima of r_{eff}. Figure 3.6 is actually not a very practical case because there is usually some loss both in traversing the passive cavity and in coupling back into the active section, and generally $r_2 \neq r_3$. Thus, the minima do not tend to be as deep, and the maxima have more shape. This is one case in nature where loss seems to help.

External cavities are not very useful for axial mode selection in the VCSEL case because their short cavities together with the finite gain bandwidth usually provides single-axial mode operation. Here lateral modes are the larger problem.

Differential efficiency through the back mirror can be calculated using $\alpha_i \cdot L_{DBR}$, where $L_{DBR} = L_c + 2L_{eff} = 1146$ nm. From Eq. (3.70),

$$\eta_d = F_2 \eta_i \frac{T_m}{T_m + A_i} = 0.349 \cdot 0.9 \frac{\ln \frac{1}{\sqrt{0.9985 \cdot 0.993}}}{1146 \cdot 10^{-7} \cdot 20 + \ln \frac{1}{\sqrt{0.9985 \cdot 0.993}}} = 0.703.$$

Figure 3.21 illustrates the results of grading the material composition (Al-fraction) and modulating the doping ($N_a - N_d$) within a period of a p-doped DBR VCSEL mirror to reduce series resistance. Also indicated is the relative position of the $|\mathscr{E}|^2$-field standing wave and the resulting hole concentration. A bi-parabolic

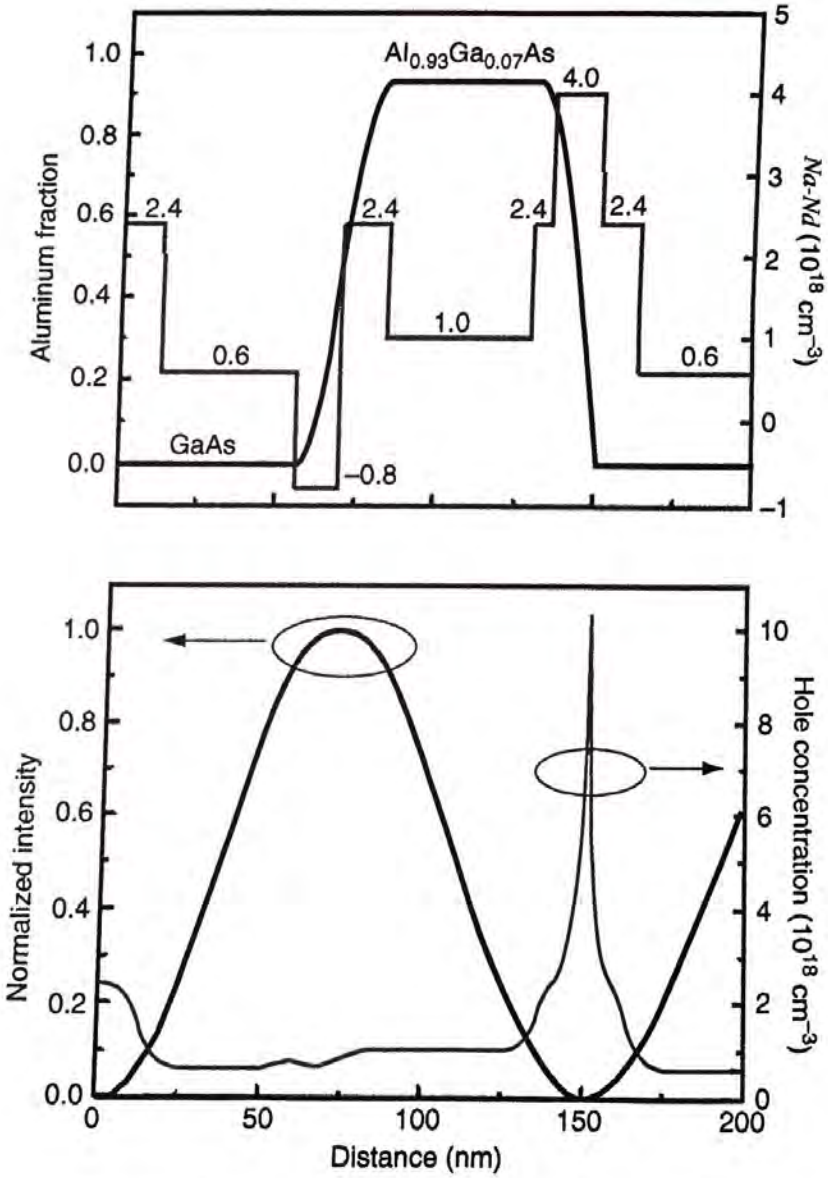

FIGURE 3.21: Illustration of bandgap engineering in a VCSEL DBR mirror—grading of composition and doping to reduce series resistance while avoiding large increases in optical losses or reduction in reflection.

When the DBR mirror section is tuned, two effects come into play, as shown in Fig. 3.23. First, the grating Bragg wavelength will change, due to the changed grating index. Then, the cavity mode comb position will change as well because the effective optical cavity length is now different. For the modal index change of $\Delta\bar{n}_{DBR}$, the center wavelength of the grating moves in direct proportion to the index according to Eq. (3.75),

$$\Delta\lambda_g = \lambda_g \frac{\Delta\bar{n}_{DBR}}{\bar{n}_{DBR}} = 1550\frac{0.01}{3.4}\ \text{nm} = 4.56\ \text{nm}.$$

At the same time, the cavity modes will shift, and we can use Eq. (3.76) to determine the amount of shift,

$$\Delta\lambda_m = \frac{\Delta\bar{n}_{DBR} L_{eff} \lambda_m}{\bar{n}_{ga}L_a + \bar{n}_{gp}L_p + \bar{n}_{gDBR}L_{eff}} = \frac{0.01 \cdot 50\ \mu\text{m} \cdot 1550\ \text{nm}}{2(3.8)(300 + 100 + 50\ \mu\text{m})} = 0.227\ \text{nm}$$

Finally, the new lasing mode will be the cavity mode that is the closest to the new Bragg wavelength. To compute it, we need to compute by how many cavity modes the Bragg wavelength shifted.

$$\Delta\lambda_{lasing} = \Delta\lambda_m + \left[\frac{\Delta\lambda_g - \Delta\lambda_m}{\delta\lambda}\right]\delta\lambda = 0.227\ \text{nm} + 6 \cdot 0.702\ \text{nm} = 4.439\ \text{nm}.$$

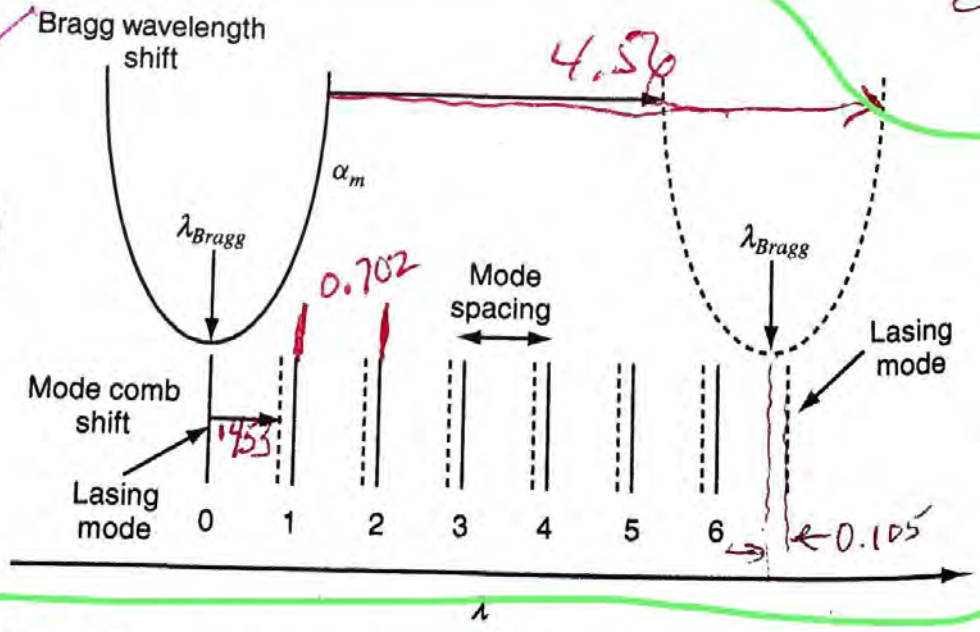

FIGURE 3.23: Illustration of mode tuning in a single-frequency three-section DBR laser. Dashed curves and lines apply after index is increased in the mirror. Two tuning effects can be observed: (1) DBR Bragg wavelength tuning, due to mirror index change and (2) cavity mode comb shift, due to its penetration into the DBR with an increased index.

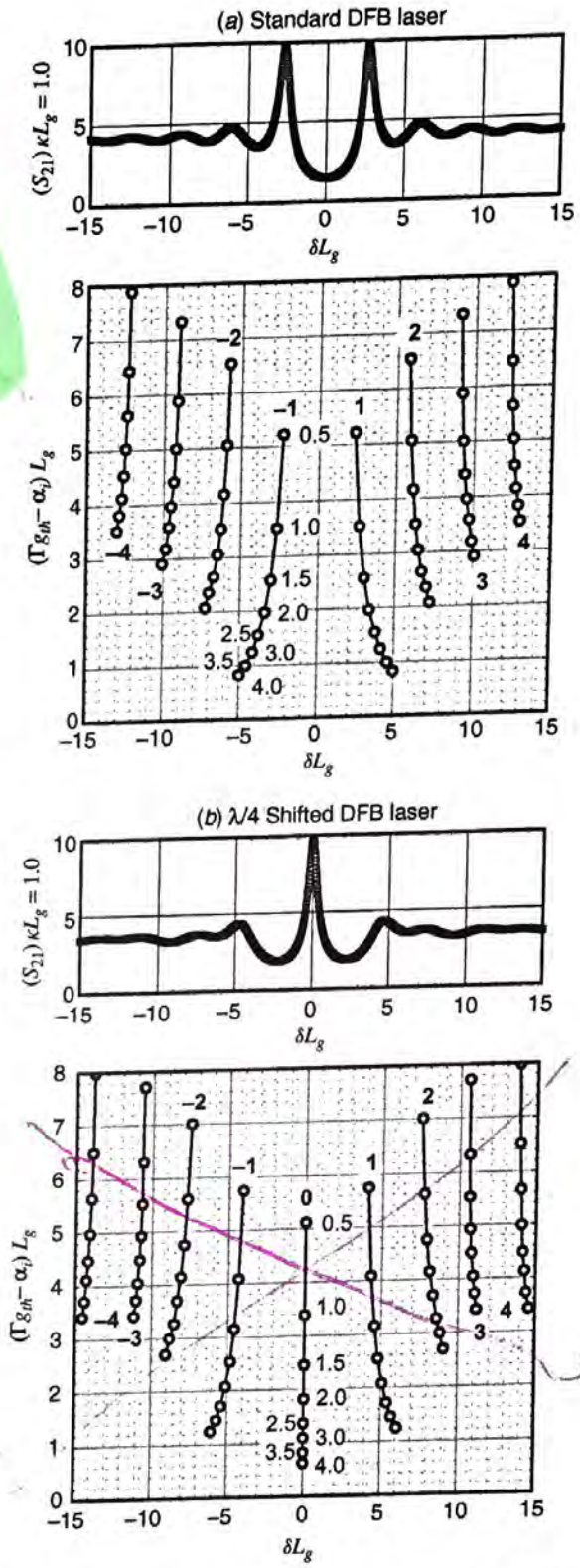

FIGURE 3.26: Example S_{21} spectra and normalized plots of threshold modal gain and threshold wavelength for different modes of (a) standard and (b) quarter-wave shifted DFB lasers. S_{21} spectra shown for $\kappa L_g = 1$ at a gain just below threshold; plots summarize analogous threshold points for this lowest order and some higher order modes with $\kappa L_g (\equiv 2mr)$ ranging from 0.5 to 4 in 0.5 increments. Here $\delta = \beta - \beta_0$, where β is the average propagation constant of the grating.

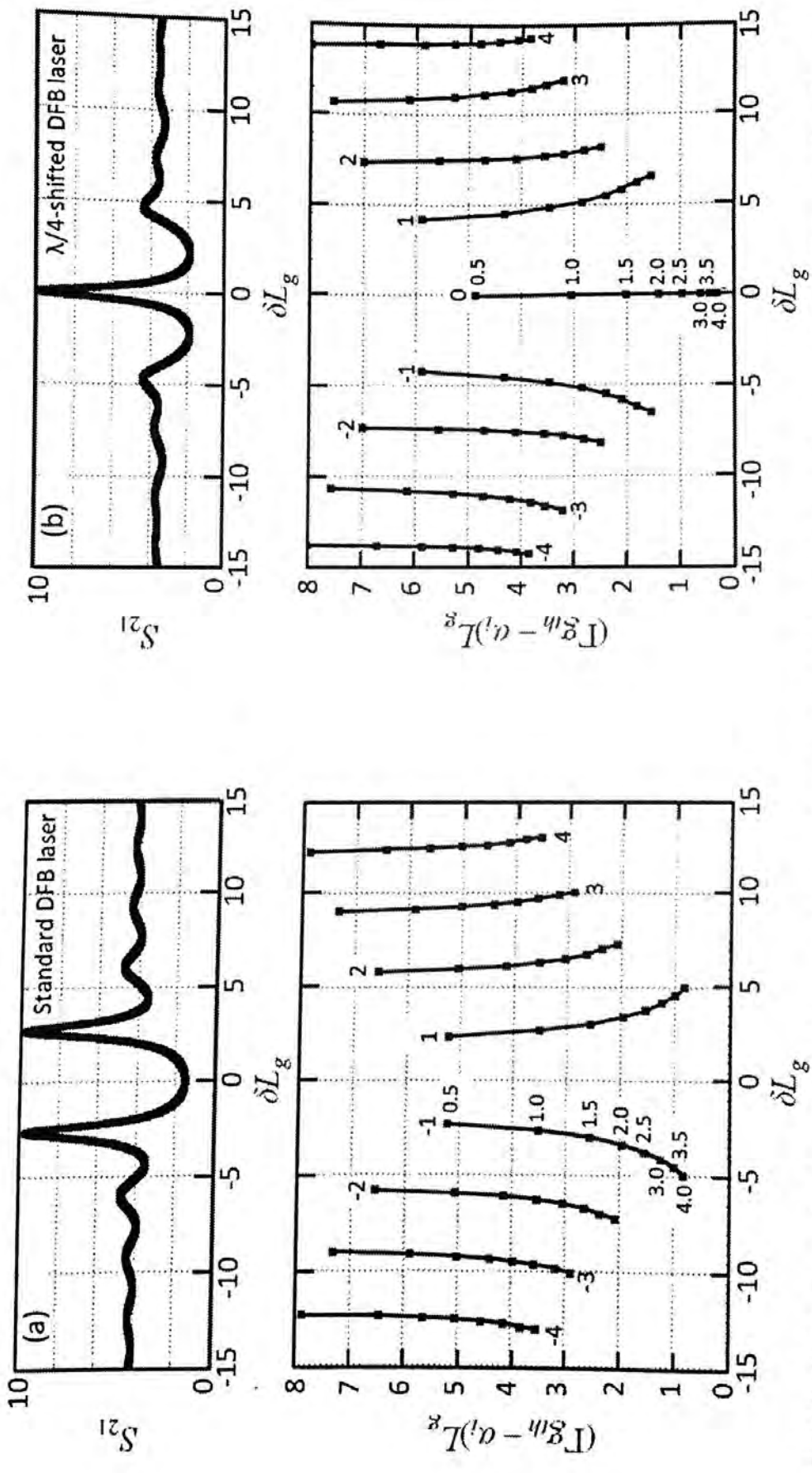

FIGURE 3.26: Example S_{21} spectra and normalized plots of threshold modal gain and threshold wavelength for different modes of (a) standard and (b) quarter-wave shifted DFB lasers. S_{21} spectra shown for $\kappa L_g = 1$ at a gain just below threshold; plots summarize analogous threshold points for this lowest order and some higher order modes with κL_g ($\equiv 2mr$) ranging from 0.5 to 4 in 0.5 increments. Here $\delta = \beta - \beta_0$, where β is the average propagation constant of the grating.

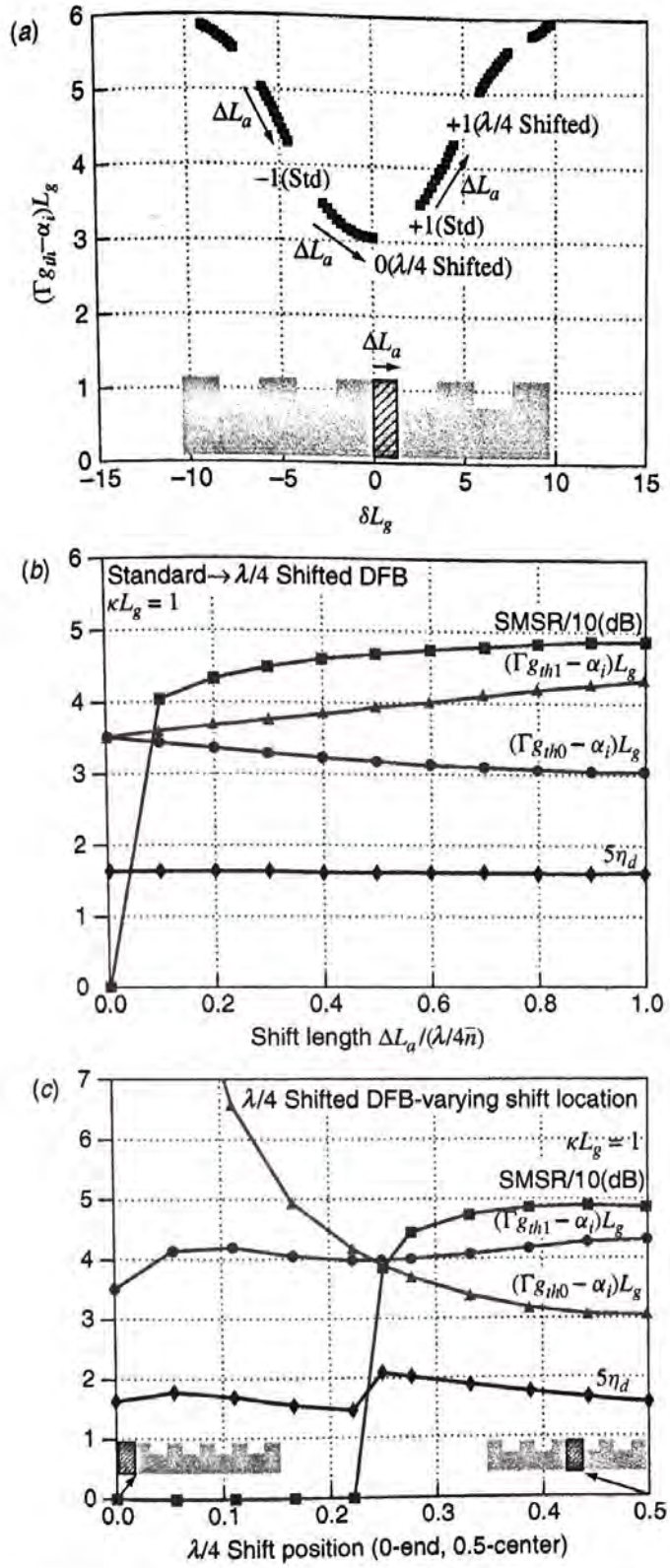

FIGURE 3.27: Characteristics of AR-coated DFBs in transition between the standard and quarter-wave-shifted designs. (a) Normalized threshold modal gain and wavelength as the shift in the center of the cavity, ΔL_a, is increased in increments of 10% of a quarter wavelength of the guided mode from 0 to full quarter-wave shift. (b) & (c) Plots of side-mode-suppression ratio, normalized modal gains for the first two modes, and differential efficiency out of the end nearest the shift; for (b) vary ΔL_g, for (c) vary position of fixed quarter-wave shift from end. Assumed cavity parameters are: $\alpha_i = 10\ \text{cm}^{-1}$, $\eta_i = 0.75$, $\beta_{sp} = 1.25 \cdot 10^{-5}$ and $\eta_r = 0.8$ (per Eq. (3.85)), $I = 4I_{th}$.

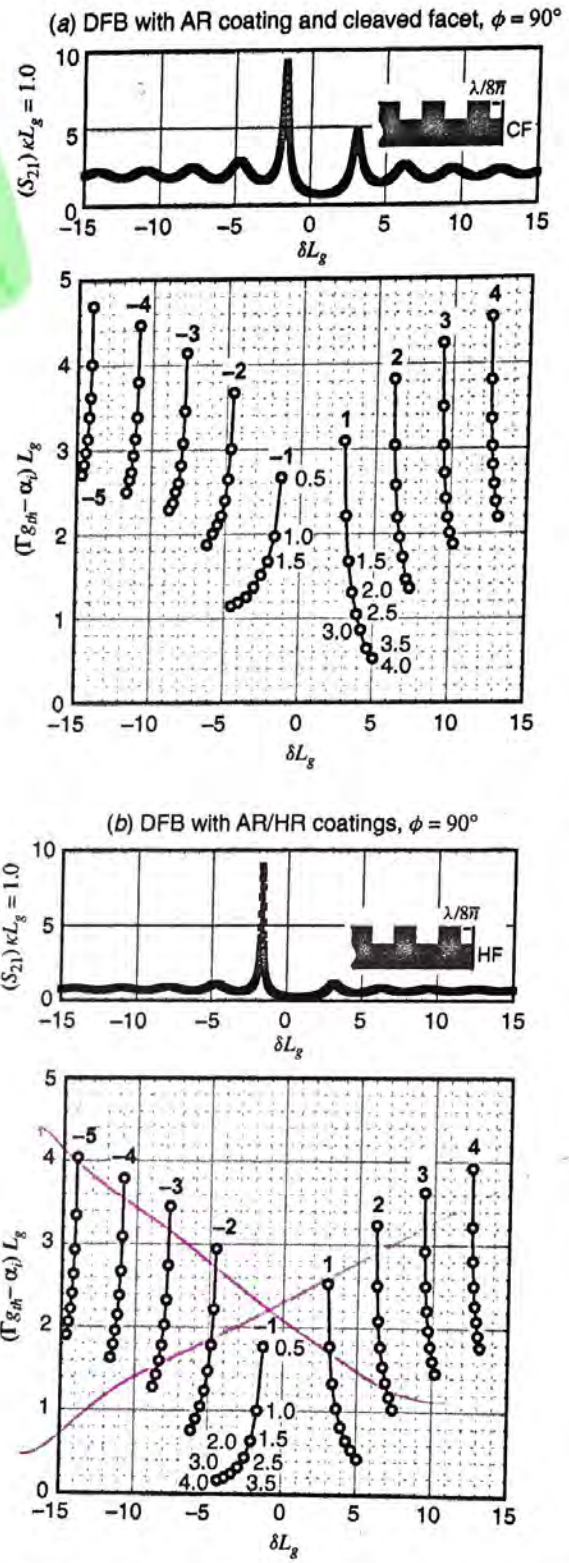

FIGURE 3.28: Example S_{21} spectra and normalized plots of threshold modal gain and threshold wavelength for different modes of a standard DFB laser with one end AR-coated and the other end either (a) a simple cleave, $R = 0.32$, or (b) HR-coated with $R = 0.9$. S_{21} spectra shown for $\kappa L_g = 1$ at a gain just below threshold; plots summarize analogous threshold points for this lowest order and some higher-order modes with $\kappa L_g\,(\equiv 2mr)$ ranging from 0.5 to 4 in 0.5 increments. The additive end reflections are optimally placed to provide orthogonally phased reflections (as illustrated by the inset).

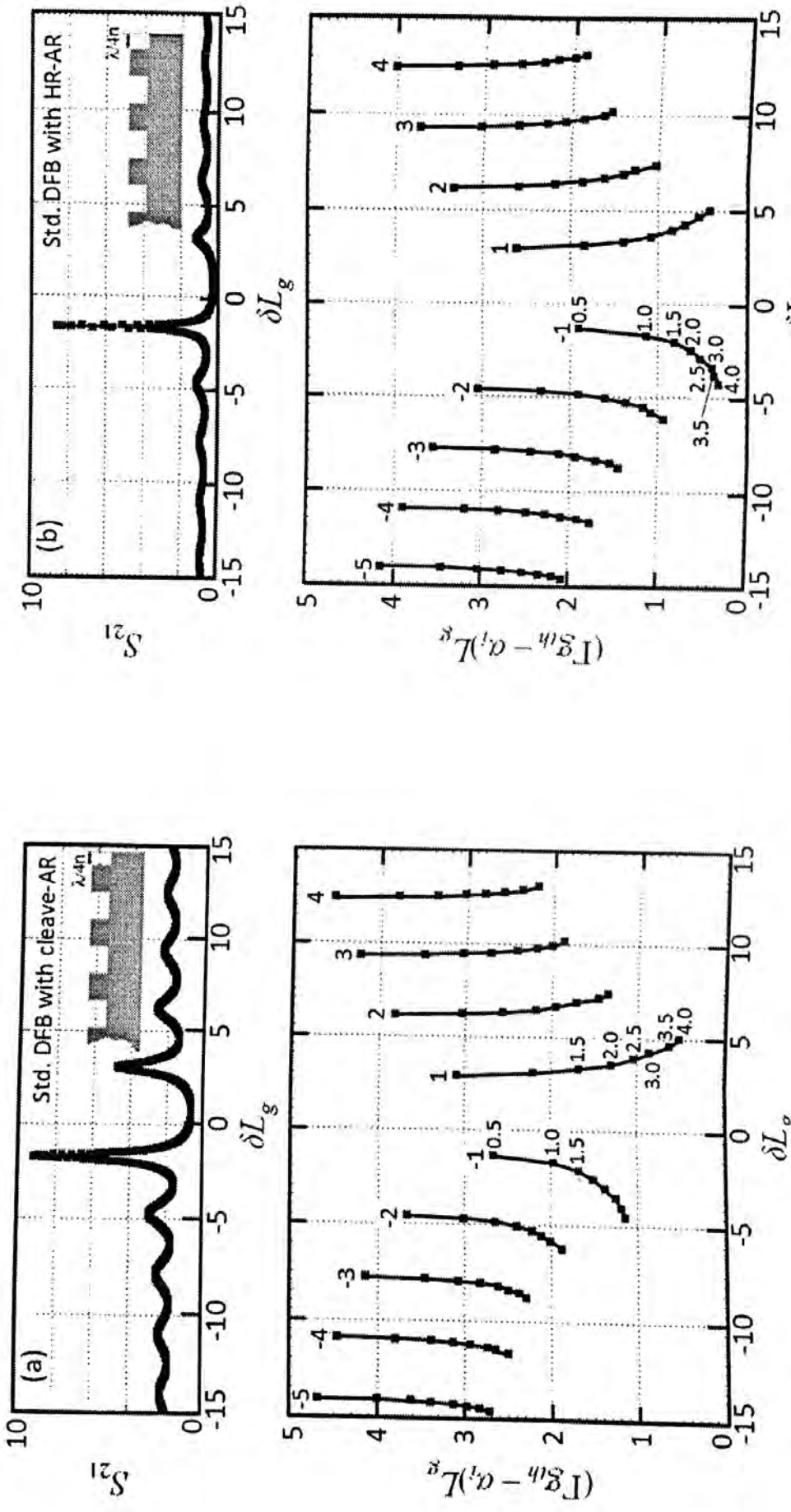

FIGURE 3.28: Example S_{21} spectra and normalized plots of threshold modal gain and threshold wavelength for different modes of a standard DFB laser with one end AR-coated and the other end either (a) a simple cleave, R = 0.32, or (b) HR-coated with R = 0.9. S_{21} spectra shown for $\kappa L_g = 1$ at a gain just below threshold; plots summarize analogous threshold points for this lowest order and some higher order modes with κL_g ($\equiv 2mr$) ranging from 0.5 to 4 in 0.5 increments. The additive end reflections are optimally placed to provide orthogonally phased reflections (as illustrated by the insets).

Problem: (1) Determine the threshold modal gain of this laser. (2) Determine the differential efficiency for this laser. (3) Determine the lasing wavelength of this laser. (4) Determine the threshold modal gain, differential efficiency and the lasing wavelength for an HR-AR standard DFB laser with the same parameters, assuming optimal HR mirror phase.

Solution: To solve this problem, we need to use Figure 3.26b, which provides us with the normalized solutions for the quarter-wave-shifted DFB mirror loss versus wavelength detuning, in function of the grating length and coupling coefficient. From the problem formulation, $\kappa L_g = 500 \cdot 20 \cdot 10^{-4} = 1.0$. Using the chart for $\kappa L_g = 1.0$,

$$A = (\Gamma g_{th} - \langle \alpha_i \rangle) L_g = 3.1 \Rightarrow \Gamma g_{th} = \frac{3.1}{L_g} + \langle \alpha_i \rangle$$

$$= \frac{3.1}{500 \cdot 10^{-4}}\ \text{cm}^{-1} + 10\ \text{cm}^{-1} = 72\ \text{cm}^{-1}.$$

For a DFB laser, the differential efficiency is given by

$$\eta_d = \eta_i \frac{A}{\Gamma g_{th} L_g} = 0.75 \frac{3.1}{72 \cdot 0.05} = 0.646,$$

where half of the power would be emitted from each end of the grating, yielding a single-sided differential efficiency of $\eta_d = 0.323$. In a quarter-wave-shifted DFB laser, the detuning of the lasing wavelength from the Bragg wavelength is zero (as seen from the chart in Figure 3.26b), so the lasing wavelength is 1550 nm.

For the HR-AR coated DFB laser, we now need to use the chart from Fig. 3.28b. We follow the same procedure. Using the chart for $\kappa L_g = 1.0$,

$$A = (\Gamma g_{th} - \langle \alpha_i \rangle) L_g = 1.2 \Rightarrow \Gamma g_{th} = \frac{1.2}{L_g} + \langle \alpha_i \rangle$$

$$= \frac{1.2}{500 \cdot 10^{-4}}\ \text{cm}^{-1} + 10\ \text{cm}^{-1} = 34\ \text{cm}^{-1}.$$

$$\eta_d = \eta_i \frac{A}{\Gamma g_{th} L_g} = 0.75 \frac{1.2}{34 \cdot 0.05} = 0.529,$$

where in this case, nearly all the power is coming out of the AR-coated facet.

Using the normalized plot of threshold modal gain and wavelength from Fig. 3.28, the normalized detuning for the lasing mode is $\delta L_g = 0.35$, therefore the lasing wavelength is

$$\Delta\lambda = -\frac{\lambda_0^2}{2\pi \bar{n}_g}\delta \qquad -1.8$$

$$\beta = \frac{2\pi}{\lambda}\bar{n} = \frac{2\pi}{\lambda_0}\bar{n} + \frac{\delta L_g}{L_g} \Rightarrow \lambda = \frac{2\pi \bar{n}}{\frac{2\pi}{\lambda_0}\bar{n} + \frac{\delta L_g}{L_g}}$$

$$= \frac{2\pi}{0.013 + 0.0000007}\ \text{nm} = 1551.087\ \text{nm}.$$

$$\Delta\lambda = -\frac{1.55^2(-1.8)}{2\pi(3.8)(500)} = 0.362 \times 10^{-3}\ \mu\text{m} \Rightarrow \lambda = 1550.362\ \text{nm}$$

that $f_2(E_{c2}) - f_1(E_{v2}) \approx 0.3 - 0.8 = -0.5$, we find that the absorption from the $n = 2$ subband transitions is $0.5g_{max2}(E_{g2})$. For the $n = 1$ subband transitions, it's a little trickier because the Fermi energies must be estimated for electrons and holes separated by E_{g2} in the $n = 1$ subbands. Using Eq. (4.30), we must evaluate $f_2[E_{c1} + (E_{g2} - E_{g1})(m_r/m_c)] - f_1[E_{v1} - (E_{g2} - E_{g1})(m_r/m_v)]$, which from the figure is approximately $\approx 0.2 - 0.7 = -0.5$. The overall absorption at the second subband edge is therefore $0.5(g_{max1}(E_{g2}) + g_{max2}(E_{g2}))$ (cross-population transitions such as g_{max12} and g_{max21} also exist but as mentioned earlier, their contributions are typically small). So we find that the absorption at E_{g2} has not yet been converted into gain but has at least been reduced to half its maximum absorption value with the application of a forward bias. To achieve gain at the $n = 2$ subband edge, the forward bias must be increased to the point where $E_{Fc} - E_{Fv} > E_{g2}$. To surpass the $n = 1$ subband edge gain, the forward bias must be even stronger such that

$$(g_{max1}(E_{g2}) + g_{max2}(E_{g2}))(f_2(E_{c2}) - f_1(E_{v2})) > g_{max1}(E_{g1})(f_2(E_{c1}) - f_1(E_{v1})).$$

So for all but very strong forward-bias conditions, the $n = 1$ gain dominates.

Quantum Dots To apply the gain theory to quantum dots, we need to take into account their special physical and quantum properties. If we assume that we have a uniform distribution of quantum dots, as shown in Fig. 4.10, 1 dot will occupy a unit volume equal to $V = L_x L_y L_z$. Each dot occupies a volume equal to $V_{dot} = d_x d_y d_z$ inside this unit volume. The three-dimensional dot density is then given by

$$\rho_{dot}^{3D} = \frac{1}{V} = \frac{1}{L_x L_y L_z}$$

The conduction band energy is given by

$$E = E_{c0} + \frac{\hbar^2 \pi^2}{2m^*}\left[\left(\frac{n_x}{d_x}\right)^2 + \left(\frac{n_y}{d_y}\right)^2 + \left(\frac{n_z}{d_z}\right)^2\right]. \tag{4.40}$$

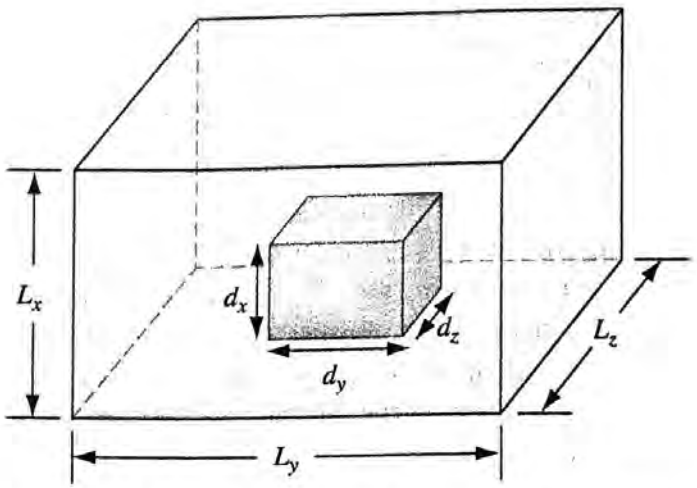

FIGURE 4.10: Quantum dots and their geometric parameters.

where N can be either the two- or three-dimensional carrier density. A common value used for the bandgap shrinkage constant in bulk material (assuming $N = P$), which also falls within the measured range for quantum well material, is

$$c \approx 32 \text{ meV}/(10^{18} \text{ cm}^{-3})^{1/3}, \quad \text{(bulk GaAs)} \tag{4.54}$$

$$c \approx 32 \text{ meV}/(10^{12} \text{ cm}^{-2})^{1/2}. \quad \text{(GaAs/AlGaAs QW)} \tag{4.55}$$

$$c \approx 20 - 25 \text{ meV}/(10^{12} \text{ cm}^{-2})^{1/2}. \quad \text{(InGaAs/InP QW)} \tag{4.56}$$

$$c \approx 10 - 20 \text{ meV}/(10^{12} \text{ cm}^{-2})^{1/2}. \quad \text{(AlGaAs/GaAs QW)} \tag{4.57}$$

$$c \approx 24 \text{ meV}/(10^{8} \text{ cm}^{-2})^{1/2}. \quad \text{(GaN QW)} \tag{4.58}$$

Equations (4.54) to (4.58) are not entirely accurate because there is some experimental uncertainty in both the one-third power law and the value of c. However, they do provide a simple and reasonable estimate of the extent of bandgap shrinkage. Less data exist for other material systems, so it is common to assume the same values in the InGaAsP system as for the GaAs/AlGaAs system.

The net effect of bandgap shrinkage is that as carrier density increases, the entire gain spectrum redshifts by a noticeable amount. In principle, the shift is accompanied by a slight distortion (i.e., reshaping and enhancement) of the spectrum. However, to first order we can neglect the distortion and simply assume that high carrier densities produce a *rigid* shift of the entire gain spectrum to longer wavelengths. This phenomenon is observable in quantum-well lasers where the high threshold carrier density shifts the lasing wavelength beyond the known band edge wavelength of the quantum well. Bandgap shrinkage is a particularly important factor in situations where there is some critical alignment between a desired cavity mode of the laser and the gain spectrum (as in a short-cavity VCSEL, for example).

4.3.5 Polarization and Piezoelectricity

For certain crystal lattice types, with particular symmetry properties and the type of bonds between atoms, large built-in electric fields are possible along certain crystal directions. This phenomenon, called piezoelectricity, occurs in the Group III nitrides arranged in the wurzite type crystal structures. III nitride wurzite crystals have a unique structure where different atom species alternate between different atomic planes, thus forming fixed charge densities at the interfaces. Spontaneous polarization, caused by atomic bond assymetry between the nearest neighbors, occurs along the growth direction of a III nitride wurtzite crystal, dictated by the substrate (this growth direction is called c axis). In addition, strain induced in these types of crystals creates a separate piezoelectric polarization field along the same axis.

For electronic devices, this polarization is largely seen as beneficial, as it gives rise to 2-D sheet concentrations at interfaces an order of magnitude higher than in other III-V systems. For LEDs and lasers (an example of a GaN barrier and InGaN quantum-well structure was shown in Fig. 1.19), the fixed sheet charges at the

volume of the box (aside from standing wave effects, which should average out over the spontaneous emission bandwidth), and we could simply set

$$V_{box}/\bar{V}_p = 1. \tag{4.68}$$

Of course, laser cavities are typically much more complex than a simple metal box, and V_p is potentially different for every optical mode. Thus, there is no guarantee that Eq. (4.50) holds in real laser cavities, or that we can even define a mode density as given in Eq. (4.66).

Fortunately, if the cavity is much larger than the wavelength of bandgap radiation in the active region, or more specifically if $V_{cav} \gg \lambda^3$, it turns out that a more rigorous treatment usually averages out to the simple metal box treatment (especially when the emission bandwidth is large relative to resonances in the cavity). To get a feel for the numbers, a typical $0.2 \times 4 \times 200\ \mu m^3$ GaAs in-plane laser has $V_{cav} \sim 10{,}000\lambda^3$. Thus, the simple metal box assumption contained in Eqs. (4.66) through (4.68) is expected to work well in this case.

In a VCSEL, the simple box assumption is more questionable. However, the volume of a typical GaAs VCSEL with dimensions of $1 \times 10 \times 10\ \mu m^3$, is smaller than a typical in-plane laser by only a factor of two, and $V_{cav} \sim 5000\lambda^3$. Thus, for VCSELs of this size, the simple box assumption should still hold. However, when the lateral dimensions of the VCSEL are reduced below 1 μm, significant deviations from the simple box assumption are expected to occur. Under these circumstances, the mode density concept must be abandoned and more sophisticated mode-counting techniques must be used to estimate the total spontaneous emission rate. In addition to mode counting, the average value for $1/\bar{V}_p$ (or equivalently $\bar{\Gamma}$) is also required. Numerous researchers interested in microcavity lasers have investigated such numerical exercises for a number of cavity geometries [18, 19].

Combining Eqs. (4.63) through (4.68) assuming the simple box assumption holds, the total spontaneous emission rate per unit energy per unit active volume (in units of $s^{-1}\ cm^{-3}\ eV^{-1}$) becomes

$$R_{sp}^{21} = \frac{1}{h}\rho_0(\nu_{21}) \cdot v_g n_{sp} \bar{g}_{21}. \tag{4.69}$$

This result is identical to Eq. (A6.32) derived in Appendix 6, with the exception that the gain here is more correctly defined as an average over all polarizations. Using the explicit expression for gain Eq. (4.33) and mode density Eq. (4.48), the general expression for spontaneous emission becomes

$$R_{sp}^{21} = \frac{4n\pi q^2}{\varepsilon_0 h^2 c^3 m_0^2} h\nu_{21} |\bar{M}_T(E_{21})|^2 \rho_r(E_{21}) \cdot f_2(1 - f_1), \tag{4.70}$$

where

$$|\bar{M}_T(E_{21})|^2 = \frac{1}{3} \sum_{\substack{\text{all three} \\ \text{polarizations}}} |M_T(E_{21})|^2.$$

To determine the total spontaneous emission power in a given wavelength range, we need know the total spontaneous emission rate over all modes that exist in that wavelength range, as well as the photon energy and the active region volume.

The total spontaneous emission per unit energy and per unit volume is given by Eq. (4.69) as $R_{sp}^{21} = \frac{1}{h}\rho_0(\nu_{21}) \cdot v_g n_{sp} \bar{g}_{21}$. To compute it, we need to compute the mode density ρ_0 and the average gain $\bar{g}_{21}$. From Appendix 4, the expression for the density of optical modes is given by Eq. (A4.5),

$$\rho_0(\nu) = \frac{8\pi}{c^3} n^2 n_g \nu^2 \Rightarrow \frac{1}{h}\rho_0(\nu) = \frac{8\pi}{(3 \cdot 10^{10}\ \text{cm/s})^3} \frac{(3.6)^2 (4.5)\left(\frac{1.24\ \text{eV}\mu\text{m}}{0.97\ \mu\text{m}}\right)^2}{\left(\frac{6.626 \cdot 10^{-34}\ \text{Js}}{1.6 \cdot 10^{-19}\ \text{J/eV}}\right)^3}$$

$$= 1.25 \cdot 10^{15}\ \text{eV}^{-1}\ \text{cm}^{-3}.$$

The average gain is given by

$$\bar{g}_{21} = \frac{1}{3}(2g_{21}^{TE} + g_{21}^{TM}) = \frac{2}{3}g_{21}^{TE} = \frac{2}{3}1986.67\ \text{cm}^{-1} = 1324\ \text{cm}^{-1},$$

because the material has been optimized for TE polarization gain only, as shown in Figure 4.4. Now, we can calculate the total spontaneous emission rate per unit volume as

$$R_{sp}^{21} = \left(\frac{1}{h}\rho_0(\nu_{21})\right) \cdot (v_g)(n_{sp})(\bar{g}_{21})$$

$$= (1.25 \cdot 10^{15}\ \text{eV}^{-1}\ \text{cm}^{-3})\left(\frac{3}{4.5} \cdot 10^{10}\frac{\text{cm}}{\text{s}}\right)(1.5)(1324\ \text{cm}^{-1})$$

$$= 1.65 \cdot 10^{28}\ \text{eV}^{-1}\ \text{cm}^{-3}\text{s}^{-1}.$$

To calculate the total power in the 1-nm bandwidth, we need to convert the bandwidth into energy and calculate the active region volume,

$$\Delta E = \Delta\lambda \frac{dE}{d\lambda} = \Delta\lambda\left(-\frac{E_p}{\lambda_p}\right) = 1\ \text{nm}\left(-\frac{1.24\ \text{eV}\mu\text{m}}{(0.97\ \mu\text{m})^2}\right) = 1.32 \cdot 10^{-3}\ \text{eV}$$

$$V_a = w \cdot d \cdot L = (3\ \mu\text{m})(8\ \text{nm})(500\ \mu\text{m}) = 12000 \cdot 10^{-15}\ \text{cm}^3.$$

Finally, the total spontaneous power emitted in the 1-nm wavelength range around the lasing wavelength is

$$P_{sptotal} = R_{sp}^{21} \cdot \Delta E \cdot h\nu \cdot V_a$$

$$= (1.65 \cdot 10^{28}\ \text{eV}^{-1}\ \text{cm}^{-3}\text{s}^{-1})(1.32 \cdot 10^{-3}\ \text{eV})\left(\frac{1.24\ \text{eV}\mu\text{m}}{0.97\ \mu\text{m}}\right)\{1.6\times10^{-19}\ \text{J/eV}\}$$

$$\times (12000 \cdot 10^{-15}\ \text{cm}^3) = 41.87\ \mu\text{W}.$$

4.4.3 Spontaneous Emission Factor

With the preceding description of spontaneous emission, we can derive a simple expression for the spontaneous emission factor used in the rate equations to express the fraction of total spontaneous emission that enters the mode of interest. Using Eq. (4.62) for the emission rate into one mode and Eq. (4.72) for the total emission rate, we have

$$\beta_{sp} \equiv \frac{R'_{sp}}{R_{sp}} = \frac{\Gamma v_g g n_{sp}}{\eta_i \eta_r I/q}, \tag{4.73}$$

where I as used here does not include stimulated emission current.

With Eq. (4.73), parameters readily accessible experimentally can be used to estimate β_{sp}. For example, assume we have a laser with a threshold current of 10 mA, a modal threshold gain of 50 cm^{-1}, and an internal efficiency of 75%. If nonradiative recombination is minimal, then $\eta_r \approx 1$. If we assume the group index is ~4 and the population inversion factor is ~1.5, we quickly find $\beta_{sp} \approx 1.2 \times 10^{-5}$, typical of experimental values measured with in-plane lasers. To get a better estimate of β_{sp}, we need to determine $c/v_g, n_{sp}$, and η_r more accurately. However, c/v_g is almost always in the range of 4–5, n_{sp} is usually between 1.25 and 1.75 for gains commonly required in lasers, and η_r is typically between 50% and 80%, implying that simple estimates of $c/v_g, \eta_{sp}$, and η_r will get us within a factor of 2 of the correct value of β_{sp}.

In a typical VCSEL, the percent gain per pass is in the range of 0.5%–1% and the cavity length is ~1 μm. This gives a modal gain of 50–100 cm^{-1}. *Radiative* threshold currents are in the range of 0.5–2.0 mA for 10 μm diameter devices. If we assume a 1 mA radiative threshold current and 100 cm^{-1} threshold modal gain, we find $\beta_{sp} \approx 1.8 \times 10^{-4}$ (assuming again that c/v_g and n_{sp} are equal to 4 and 1.5). This is about an order of magnitude higher than β_{sp} observed in typical in-plane lasers. The main difference lies in the reduction of the threshold current, which is in turn predominantly due to the reduction in active-region volume possible with VCSEL structures.

Equation (4.73) also reveals that β_{sp} is not a constant, but is dependent on the injection level. As the injection level increases, the spontaneous emission into one mode saturates at a maximum value just as the gain saturates at g_{max}. Meanwhile the current and total spontaneous emission rate continue to increase as the spectrum broadens to include more modes in the emission process. The net effect is that β_{sp} decreases with increasing injection level. In rate equation analyses, β_{sp} is often approximated as a constant (see Chapters 2 and 5). This is justified for near- and above-threshold analyses, as long as the value assumed for β_{sp} is the actual value that would exist near the threshold injection level.

4.4.4 Purcell Effect

As the cavity dimensions become small, the optical mode density departs from its simple bulk form, just as in the case of quantum wells and dots for the electronic

width of the active region in the in-plane laser depicted in Fig. 4.19. For this case, we can define two distance regions: one beneath the contact within w where we assume a uniform current injection profile, and the region outside w where there is no current injection. Mathematically, with $x = 0$ defined as the center of the stripe, we have $I(x) = I_0$ for $x < w/2$, and $I(x) = 0$ for $x > w/2$. In fabricating the laser we can either leave the active region in place outside the stripe, or we can remove it by etching through the active region outside the contact area. The first case leads to carrier outdiffusion, whereas the second case leads to surface recombination. We would like to compare these two cases.

Problem: (1) With the active region in place away from the contact, carriers are free to diffuse outside the stripe width. Solve for the concentration of the carriers $N(x)$ in and out of the stripe assuming the carrier density and its derivative (i.e., the diffusion current) are constant across the $x = w/2$ boundary. Solve for the carrier profile in this case. (2) With the active region etched away, the carriers recombine at the surface, solve for the concentration of the carriers $N(x)$ under the stripe assuming the diffusion current (defined by the slope of the carrier density) is equal to the surface recombination current, $D_{np}dN/dx = -v_s N$, at the $x = w/2$ boundary. Place your result in terms of the diffusion equivalent surface recombination velocity, $v_{sD} = \sqrt{D_{np}/\tau_{np}}$. Solve for the carrier profile in this case.

Solution: From the carrier diffusion equation (4.111), we can express the carrier concentration as

$$\frac{d^2N(x)}{dx^2} - \frac{N(x)}{D_{np}\tau_{np}} = -\frac{I(x)}{qVD_{np}}. \tag{4.88}$$

If we define $x = 0$ as the lateral center of the laser stripe, we then have that

$$I(x) = \begin{cases} I_0 & |x| \le \left|\frac{W}{2}\right| \\ 0 & |x| > \left|\frac{W}{2}\right|. \end{cases} \tag{4.89}$$

If we define $L = \sqrt{D_{np}\tau_{np}}$ and $G = \frac{I(x)}{qVD_{np}}$, then the carrier diffusion equation can be rewritten as

$$\frac{d^2N(x)}{dx^2} - \frac{N(x)}{L^2} = -G.$$

This is a special simplified form of the second order linear partial differential equation, whose solutions can be expressed analytically.

For $|x| < \left|\frac{W}{2}\right|$, within the stripe width, the carrier diffusion equation has a solution of

$$N(x) = A\cosh\left(\frac{x}{L}\right) + GL^2$$

because the solution needs to be symmetric about $x = 0$, due to the statement of the problem. A will be determined by matching the boundary conditions.

For this active material, the bandgap energy is $E_g = 800$ meV. At 300 K,

$$C(300\text{ K}) = 6 \cdot 10^{-29}\ \text{cm}^6/\text{s} = C_0 \cdot e^{-\frac{80}{26}},$$

where $kT = 26$ meV at room temperature. Finally,

$$C(340\text{ K}) = C(300\text{ K}) \cdot e^{\frac{80}{26}\cdot\frac{40}{300}} = 1.507 \cdot C(300\text{ K}) = 9.042 \cdot 10^{-29}\ \text{cm}^6/\text{s}.$$

Theoretical models attempting the preceding procedure were first considered by Beattie and Landsberg in their pioneering 1959 paper on Auger recombination [29]. Since that time researchers have applied more refined versions of the theory to various material systems. Dutta and Nelson [30] analyzed the InGasP system, whereas Takeshima [32] also analyzed AlGaAs and other systems. Van de Walle analyzed InGaN-based systems using density-functional theory with many body perturbation theory [31]. Taylor et al. [39] as well as others have attempted to extend the theory to quantum wells and quantum-wire material. Unfortunately, the difficulty with theories of Auger recombination is that information of the band structure at more than a bandgap away from the band edge must be known accurately. Overlap integrals of "k-space distant" Bloch functions must also be known. Such experimental information is sparse, and theories are inevitably led to making very simplifying assumptions. In contrast, the spontaneous emission rate considered in Section 4.4 can be obtained from the band edge Bloch function overlap and band edge curvatures, data that is experimentally abundant. Hence, spontaneous emission rate calculations can be quite accurate.

In general, theories can predict the Auger rate to within an order of magnitude. That is not to say they are not important. On the contrary, they remain valuable for predicting trends in the Auger recombination rate, such as the temperature and bandgap dependence. Also, the *relative* effects of material composition variations and of reduced dimensionality can be estimated theoretically. In addition, the relative importance of the three Auger processes can be determined. Most Auger theories predict that the CHHS process dominates in common III–V semiconductors, with the CCCH process almost an order of magnitude smaller (however, some theories estimate comparable magnitudes for these two processes). The CHHL process is orders of magnitude smaller than either the CHHS or CCCH process and its contributions are negligible.

Continued refinements in the theory can hopefully produce more accurate predictions. For example, Takeshima [32] has enhanced the accuracy of his Auger theory by using realistic band structures. His model extends deep into both conduction and valence bands, accounting for the nonparabolicity in all bands. In addition the band model includes the anisotropy of the band structure (the change in the band curvature along different directions of the crystal), which he considers a very important factor. His predictions include phonon-assisted Auger processes implicitly, which he finds also to be important in InGaAsP material, contrary to the results of other

the measured differential gain depending on the threshold carrier density of the laser). In both material systems, the strained QWs yield a ~50% improvement over unstrained QWs. The bulk values in both cases are the lowest, coming in at below 5×10^{-16} cm^2. In the InP system, *dg/dN* is highest at both extremes of strain and dips by about one-third in between these extremes. The secondary peak on the GaAs QW *dg/dN* curve corresponds to the peak gain switching to the C–LH (11) transition, which rides on top of the C–HH (11) transition at slightly shorter wavelengths (see Fig. 4.24).

Example 4.7 The GaAs/AlGaAs quantum-well active material from Table 4.4 is part of a 5 quantum-well-stack-based material used to fabricate an 800-μm-long and 3-μm-wide ridge laser. The transverse confinement factor Γ_{xy} is 5.5%. From the parameter extraction, the average internal losses are determined to be $\alpha_i = 14$ cm^{-1}, and the injection efficiency is $\eta_i = 0.75$.

Problem: Determine the threshold current for this laser and compare the contributions from spontaneous and nonradiative threshold current components.

Solution: The threshold modal gain of this all-active laser is given by

$$\Gamma g_{th} = \langle \alpha_i \rangle + \frac{1}{L} \ln\left(\frac{1}{R}\right) = 14 \text{ cm}^{-1} + \frac{10^4}{800} \ln\left(\frac{1}{0.32}\right) \text{cm}^{-1} = 28.24 \text{ cm}^{-1}.$$

To calculate the threshold current, we first need to calculate the threshold carrier density using the Eq. (2.48). Because we are dealing with a GaAs-based material system, we only need to take into account the radiative threshold current component, given by Eq. (2.51). However, we need to compare the two current components and thus need to calculate the nonradiative threshold current as well, given by Eq. (2.52). Using the two-parameter fit from Table 4.4 and Eq. (2.48), the threshold carrier density is

$$N_{th} = N_{tr} e^{\frac{g_{th}}{\beta_0 N}} = 2.6\, e^{\frac{28.24}{0.055 \cdot 2400}} \cdot 10^{18} \text{ cm}^{-3} = 3.22 \cdot 10^{18} \text{ cm}^{-3}.$$

The volume of the active region consists of five 8-nm-wide quantum wells, bound by the laser facets and the ridge width,

$$V = L \cdot W \cdot N_w \cdot d = 800 \cdot 3 \cdot 5 \cdot 0.008 \cdot 10^{-12} \text{ cm}^3 = 96 \cdot 10^{-12} \text{ cm}^3.$$

Finally, the threshold current is given by

$$I_{th} = \frac{qV}{\eta_i}(BN_{th}^2 + CN_{th}^3) = \frac{1.602 \cdot 10^{-19} \cdot 96 \cdot 10^{-12} \text{ cm}^3}{0.75} \times (10.37 \cdot 10^{26} + 1.334 \cdot 10^{26})\text{A} = 24 \text{ mA},$$

where $B = 1 \cdot 10^{-10}$ cm^3/s and $C = 4 \cdot 10^{-30}$ cm^6/s.

The contribution from the Auger nonradiative current is $\frac{1.334}{11.704} = 11.4\%$.

g_{0N} to be twice as large as g_{0J}. In comparing the two-parameter fits in Tables 4.4 and 4.5, we see that this is true to an extent.

Example 4.8 Table 4.5 gives two-parameter fit data for the material gain of 1% compressively strained 3-nm thick 1.55-μm quantum-well on Indium Phosphide that neglect Auger recombination. Now, we would like to include an Auger coefficient, determined in ~~Example 4.5~~. Fig. 4.31.

Problem: Determine the new J_{tr} and g_0 that would best model the gain curve for the gains between 500 and 2500 cm^{-1}.

Solution: To solve this problem, we need to compute g_{02} and J_{tr2} of the new logarithmic relationship between the gain and current density. To accomplish this, we need to calculate the current densities for two different values of gain. The new current density is given by $J_2 = J_1 + J_A$, where $J_A = \frac{q \cdot C \cdot N^3 \cdot V}{area} = q \cdot d \cdot C \cdot N^3$. From Table 4.5, we have that $g_{01} = 2600\ cm^{-1}$ and $J_{tr1} = 13\ A/cm^2$, and the quantum well width $d = 3$ nm. Because we also know the carrier density versus gain dependence for this material from Table 4.4, $g = g_{0N} \ln \frac{N}{N_{tr}}$, and $g_{0N} = 4000\ cm^{-1}$ and $N_{tr} = 3.3 \cdot 10^{18}\ cm^{-3}$, we are in a position to calculate the total current density. At transparency, $g = 0$, we have

$$J_{tr2} = J_{tr1} + J_{Atr} = 13\ A/cm^2 + q \cdot d \cdot CN_{tr}^3 = (13 + 103)\ A/cm^2.$$

At $J_1 = e \cdot J_{tr1}$, we have

$$g = g_{01} \ln \frac{e \cdot J_{tr}}{J_{tr}} = g_{01} = 2600\ cm^{-1}, N = N_{tr} e^{\frac{g}{g_{0N}}}$$

$$= 3.3 \cdot 10^{18} e^{\frac{2600}{4000}}\ cm^{-3} = 6.32 \cdot 10^{18}\ cm^{-3}.$$

From here,

$$J_A = q \cdot d \cdot C \cdot N^3$$

$$= (1.6 \cdot 10^{-19} C)(3 \cdot 10^{-7}\ cm)(6 \cdot 10^{-29}\ cm^6/s)(6.32 \cdot 10^{18}\ cm^{-3})^3 = 727\ A/cm^2$$

and finally

$$J_2 = e \cdot J_{tr1} + J_A = 762\ A/cm^2.$$

Now, g_{02} can be calculated from the transparency current,

$$g_{02} = \frac{g_{01}}{\ln \frac{J_2}{J_{tr2}}} = \frac{2600\ cm^{-1}}{\ln \frac{762}{116}} = 1381\ cm^{-1}.$$

the carriers over a larger energy range for a given overall carrier density. The result is a lower spectral concentration of inverted carriers, which leads to a broadening and flattening of the gain spectrum.

In in-plane semiconductor lasers, the threshold current generally increases exponentially with temperature. As discussed in Chapter 2, this dependence is commonly characterized by

$$I_{th} \sim e^{T/T_0} \rightarrow T_0 = \frac{T_2 - T_1}{\ln(I_2/I_1)}, \tag{4.110}$$

where T_0 is a parameter that characterizes the thermal behavior of the threshold current of the laser. The second equation allows one to estimate T_0 from two threshold measurements at two different temperatures. By comparing the two sets of gain curves in Fig. 4.35, it is evident that InP-based materials are affected by temperature more than GaAs-based materials. Measurements yield a value of T_0 ~50–100 K for InP-based in-plane lasers and a value of $T_0 \sim$ 100–150 K for GaAs-based in-plane lasers. These values are smaller than the theoretical curves in Fig. 4.35 would suggest. However, there are other temperature-dependent effects. For example, the Auger coefficient itself is temperature-dependent, and as the latter part of Appendix 2 reveals, carrier leakage out of the active region is also very sensitive to temperature.

Example 4.9 For an InP the laser based on the material from Example 4.6, we would like to estimate the performance at 340 K, knowing that the radiative efficiency, given as the ratio between the radiative and total threshold current, is $\eta_r = \frac{I_{RAD}}{I_A + I_{RAD}} = 0.134$ at 300 K.

Problem: (1) Determine the ratio of the threshold current at 340 K/300 K, assuming only Auger nonradiative recombination, and that the required threshold carrier density increases by 10% as the temperature is raised from 300 to 340 K. (2) What is the characteristic temperature T_0 for this laser's threshold current?

Solution: From the problem statement, we have that the threshold current is given by the sum of the radiative and Auger components, $I_{th} = qV(BN^2 + CN^3) = I_{RAD} + I_A$. At 340 K, $N(340\text{ K}) = 1.1N(300\text{ K}), B(340\text{ K}) = B(300\text{ K})$, and $C(340\text{ K}) = 1.436 \cdot C(300\text{ K})$. At 340 K,

$$\frac{\Delta I_{th}}{I_{th}} = \eta_r \left(\frac{\Delta I_{RAD}}{I_{RAD}}\right) + (1 - \eta_r)\left(\frac{\Delta I_A}{I_A}\right).$$

The change in the radiative current is caused by the change in the carrier concentration, $\Delta I_{RAD} = ((1.1)^2 - 1) \cdot I_{RAD}$, whereas the change in the Auger current is caused by both the carrier concentration, and the Auger coefficient change, $\Delta I_A = ((1.1)^3 \cdot 1.436 - 1) I_A$. Finally,

$$\frac{\Delta I_{th}}{I_{th}} = 0.134 \cdot (0.21) + 0.866 \cdot (0.911) = 0.817.$$

From here, we have that

$$\frac{I_{th}(340\text{ K})}{I_{th}(300\text{ K})} = \frac{\Delta I_{th} + I_{th}}{I_{th}} = 1.817 = e^{\frac{40\text{ K}}{T_0}}$$

and finally $T_0 = \frac{40\text{ K}}{\ln 1.817} = 70\text{ K}$.

REFERENCES

1. Hermann C, Weisbuch C. $\vec{k}\cdot\vec{p}$ perturbation theory in III-V compounds and alloys: a reexamination. *Phys Rev B* 1977;**15**: 823.
2. Hermann C, Weisbuch C. *Modern problems in condensed matter sciences*. Volume 8, Optical orentation, ed. Agranovich VM, Maradudin AA. Amsterdam: North-Holland; 1984. p 463–508.
3. Jani B, Gibart P, Portal JC, Aulombard RL. Effective masses in Sn-doped $Ga_{1-x}Al_xAs$ ($x < 0.33$) determined by the Shubnikov–de Haas effect. *J Appl Phys* 1985;**58**: 3481.
4. Nicholas RJ, Portal JC, Houlbert C, Perrier P, Pearsall TP. An experimental determination of the effective masses for $Ga_xIn_{1-x}As_yP_{1-y}$ alloys grown on InP. *Appl Phys Lett* 1979;**34**: 492.
5. Casey HC Jr, Panish MB. *Heterostructure lasers, part A: fundamental principles*. Orlando, FL: Academic Press; 1978. For bandgap shift, see also Camassel J, Auvergne D, Mathieu H. Temperature dependence of the band gap and comparison with the threshold frequency of pure GaAs lasers. *J Appl Phys* 1975;**46**: 2683.
6. Kaminow IP, Li T, Willner AE. *Optical fiber telecommunications V A—components and subsystems*. Amsterdam: Elsevier; 2008.
7. Yamada M, Ishiguro H, Nagato H. Estimation of the intra-band relaxation time in undoped AlGaAs injection laser. *Jpn J Appl Phys* 1980;**19**: 135.
8. Yamanishi M, Lee Y. Phase dampings of optical dipole moments and gain spectra in semiconductor lasers. *IEEE Journal of Quantum Electronics* 1987;**QE-23**: 367.
9. Asada M. Intraband relaxation effect on optical spectra. In: Zory PS Jr, editor. *Quantum well lasers*. San Diego: Academic Press; 1993. Chap. 2.
10. Kucharska AI, Robbins DJ. Lifetime broadening in GaAs-AlGaAs quantum well lasers. *IEEE Journal of Quantum Electronics* 1990;**QE-26**: 443.
11. Chinn SR, Zory P, Reisinger AR. A model for GRIN-SCH-SQW diode lasers. *IEEE Journal of Quantum Electronics* 1988;**QE-24**: 2191.
12. Tarucha S, Kobayashi H, Horikoshi Y, Okamoto H. Carrier-induced energy-gap shrinkage in current-injection GaAs/AlGaAs MQW heterostructures. *Jap J Appl Phys* 1984;**23**: 874. Also see Tomita A, Suzuki A. Carrier-induced lasing wavelength shift for quantum well laser diodes. *IEEE Journal of Quantum Electronics* 1987;**QE-23**: 1155.
13. Piprek J. *Semiconductor optoelectronid devices: introduction to physics and simulation*. San Diego, CA: Academic Press; 2003.
14. Zhao H, Arif RA, Tansu N. Self-consistent gain analysis of type-II "W" InGaN–GaNAs quantum well lasers. *J Appl Phys* 2008;**104**: 043 104–.
15. Chuang SL. *Physics of photonic devices*. Hoboken, NJ: Wiley; 2009.

section of the active region, particularly when the active width is narrow. In this problem, the effects of a finite diffusion constant for carriers in the active region will be examined.

Assume that the carrier densities in the active region are high enough that any differences in the diffusion profiles of electrons and holes will set up an electric field that will pull the two densities to nearly the same profile. In this *ambipolar* diffusion limit, the hole diffusion rate is enhanced by a factor of ~2 by the forward pull of the electrons, and the electron diffusion rate is limited to approximately twice the normal hole diffusion rate by the backward pull of the holes. The overall effect is that we can assume the electron and hole densities are equal everywhere in the active region and are characterized by a single ambipolar diffusion constant, D_{np}. The lateral profile of carriers is then governed by the simple diffusion equation:

$$D_{np}\frac{d^2N(x)}{dx^2} = -\frac{I(x)}{qV} + \frac{N(x)}{\tau_{np}}. \tag{4.112}$$

The carrier lifetime is in general a function of N; however, to obtain analytic solutions, we can evaluate the lifetime at the broad-area threshold value, $\tau_{np}|_{th} = qL_zN_{th}/J_{th}$.

The problem we wish to solve is the carrier density profile across the width of the active region in the in-plane laser depicted in Fig. 4.19. For this case, we can define two distance regions: one beneath the contact within w, where we assume a uniform current injection profile, and the region outside w where there is no current injection. Mathematically, with $x = 0$ defined as the center of the stripe, we have $I(x) = I_0$ for $x < w/2$, and $I(x) = 0$ for $x > w/2$. In fabricating the laser we can either leave the active region in place outside the stripe, or we can remove it by etching through the active region outside the contact area. The first case leads to carrier outdiffusion, whereas the second case leads to surface recombination. We would like to compare these two cases.

(a) With the active region in place away from the contact, carriers are free to diffuse outside the stripe width. Draw a sketch of this configuration and solve Eq. (4.112) for $N(x)$ in and out of the stripe assuming the carrier density and its derivative (i.e., the diffusion current) are constant across the $x = w/2$ boundary. Qualitatively sketch $N(x)$.

(b) With the active region etched away, the carriers recombine at the surface. Draw a sketch of this configuration and solve Eq. (4.112) for $N(x)$ under the stripe, assuming the diffusion current (defined by the slope of the carrier density) is equal to the surface recombination current, $D_{np}dN/dx = -v_sN$, at the $x = w/2$ boundary. Place your result in terms of the diffusion equivalent surface recombination velocity, $v_{sD} = \sqrt{D_{np}/\tau_{np}}$. Qualitatively sketch $N(x)$. In comparing $N(x)$ in (ii) to $N(x)$ in (i), what is the significance of v_{sD}? Show that Eq. (4.78) is recovered in the limit of $D_{np} \to \infty$.

Assuming an injection current of 166.4 A/cm^2 (corresponding to the broad-area threshold in Fig. 4.18) and a stripe width of 2 μm, plot $N(x)$ on

Example 5.2 For the VCSEL from Example 5.1, the plot of M/m as a function of $1/f_m$ is found to decrease for low frequencies, and then saturate at a value of 2.5 for high modulation frequencies.

Problem: What is the linewidth enhancement factor for this laser?

Solution: (a) The relationship between the FM-to-IM modulation index and the linewidth enhancement factor is given by Eq. (5.78),

$$\frac{M}{m} = \frac{\alpha}{2}\sqrt{\left(\frac{\gamma_{PP}}{\omega}\right)^2 + 1}.$$

For high modulation frequencies, the expression under the square root reduces to 1, and the value from the plot corresponds to $\frac{1}{2}$ of the enhancement factor α, therefore,

$$\alpha = 5.$$

So far we have only considered changes in the index created by the modulation of the carrier density. However, at low modulation frequencies the temperature of the laser is also modulated when we apply current modulation. Because the index varies with temperature, we should expect the frequency modulation to be affected by thermal effects as well. The total FM of the laser may therefore be written as the sum of two contributions:

$$\frac{\nu_1}{I_1} = \left(\frac{\Delta\nu}{\Delta I}\right)_{carrier} + \left(\frac{\Delta\nu}{\Delta I}\right)_{thermal} \tag{5.79}$$

where

$$\left(\frac{\Delta\nu}{\Delta I}\right)_{carrier} = \frac{\alpha}{4\pi}\frac{\eta_i}{qV_p}\frac{\varepsilon}{1+\varepsilon N_p}\cdot(1+j\omega/\gamma_{PP})H(\omega),$$

$$\left(\frac{\Delta\nu}{\Delta I}\right)_{thermal} = \frac{(1-\eta_{wp})V_{th}Z_T\ d\nu/dT}{1+j\omega\tau_T}.$$

In the first equation we have again set $\gamma_{PP} \approx \Gamma v_g a_p N_p$, expanded a_p using Eq. (5.31), and set $1/\tau_p = \Gamma v_g g$, which is a good approximation above threshold. In the second equation, η_{wp} is the well-plug efficiency of the output power P_{out}/P_{in}, Z_T is the thermal impedance of the laser structure discussed in Chapter 2, and V_{th} is the threshold voltage of the laser that is assumed roughly constant above threshold. Also τ_T is the thermal time constant, which is typically in the few microseconds range, yielding thermal cutoff frequencies in the few hundred kilohertz range. Finally, $d\nu/dT = -(c/\lambda^2)d\lambda/dT$ is the shift in the mode frequency with temperature. For 1 μm emission lasers, $d\lambda/dT \sim 0.06$–0.08 nm/K, which translates into $d\nu/dT \sim -20$ GHz/K.

For a thermal impedance of 0.1 K/mW, the *temperature* tuning below the thermal cutoff frequency is ~ -2 GHz/mA (assuming $(1-\eta_{wp})V_{th} \approx 1V$). For a VCSEL

response of the laser cavity. The Fourier transform of an exponential is a Lorentzian. This undriven result, sometimes called the cold cavity response, is given by

$$|\mathscr{E}(\omega)|^2 = \frac{|\mathscr{E}(\omega_0)|^2}{1 + (\omega - \omega_0)^2(2\tau_p)^2}. \tag{5.120}$$

From this we can see that the full-width half-maximum (FWHM) linewidth of the cold cavity is $\Delta\omega = 1/\tau_p$. This spectral width corresponds to the filter bandwidth of the Fabry–Perot resonator mode with no active material present (hence cold cavity response). The key point here is that the resonance width is linked with the photon decay rate. Now, if we add back the stimulated term that is responsible for gain in the cavity, we see from Eq. (5.4) that the same exponential solution in time is obtained, but it is now characterized by a new *effective* cavity lifetime:

$$\frac{1}{\tau_p'} = \frac{1}{\tau_p} - \Gamma v_g g. \tag{5.121}$$

The effective cavity lifetime *increases* as the gain in the cavity compensates for cavity losses. Thus with gain, the FWHM linewidth becomes $\Delta\omega = 1/\tau_p'$, and so as τ_p' increases, the resonance width decreases. As illustrated in Section 5.2.2, Eq. (5.4) can be solved in the steady state for N_p:

$$N_p = \frac{\Gamma R_{sp}'}{1/\tau_p - \Gamma v_g g}. \tag{5.122}$$

Using Eq. (5.113) to replace $[1/\tau_p - \Gamma v_g g]$ in Eq. (5.112), we can express the driven FWHM linewidth as

$$\Delta\nu_{spon} = \frac{1}{2\pi\tau_p'} = \frac{\Gamma R_{sp}'}{2\pi N_p}. \quad \text{(spontaneous only)} \tag{5.123}$$

Equation (5.123) is equivalent to the famous Schawlow–Townes linewidth formula [6]. One central conclusion of this formula is that the linewidth varies inversely with photon density (or output power). And because the photon density in a laser can grow very large, the linewidth can collapse into a very narrow spectral line—one of the defining characteristics of lasers.

Unfortunately, this intuitive derivation has some shortcomings. Equation (5.123) does correctly give the below-threshold linewidth and is therefore accurate for amplified spontaneous emission problems. However, above threshold, the nonlinear coupling between the rate equations suppresses one of the two quadrature components of the noise (the field amplitude fluctuations are stabilized above threshold), resulting in a factor of 2 reduction in the linewidth predicted here [7, 8]. With a correction factor of 1/2, Eq. (5.123) becomes the *modified* Schawlow–Townes linewidth formula:

$$(\Delta\nu)_{ST} = \frac{\Gamma R_{sp}'}{4\pi N_p}. \tag{5.124}$$

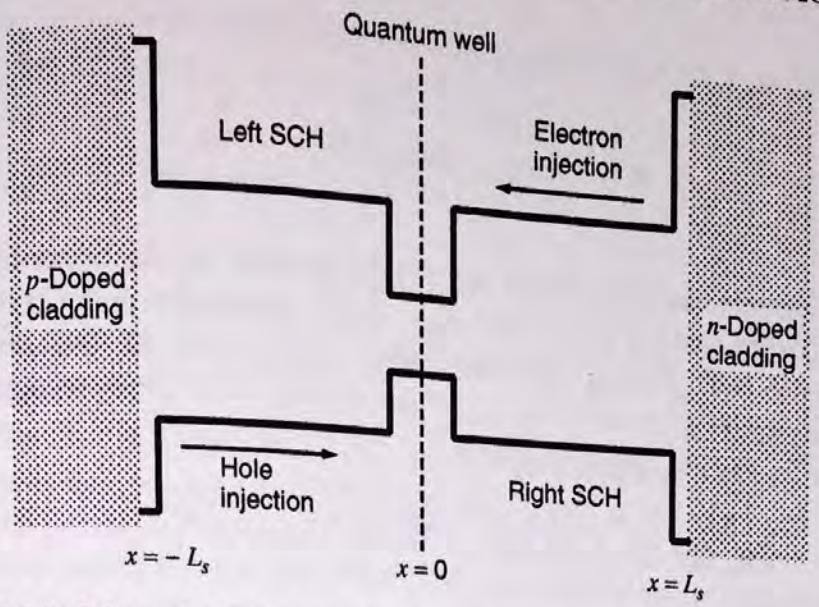

FIGURE 5.24: Schematic diagram of a single quantum-well laser with a separate-confinement heterostructure (SCH) used in the carrier transport model.

to the SCH region, and the other symbols are as defined before. In this simplified treatment, we ignore the fact that the holes come from one side of the junction and the electrons from the other. Fortunately, other more in-depth treatments, which include holes and electrons separately yield essentially the same results as this simplified analysis.

Limiting our attention to small-signal perturbations, we can linearize the rate equations as we did in Section 5.3 to obtain the differential rate equations. In matrix form, these become

$$\frac{d}{dt}\begin{bmatrix} dN_B \\ dN \\ dN_p \end{bmatrix} = \begin{bmatrix} -\gamma_{BB} & \gamma_{BN} & 0 \\ \gamma_{NB} & -\gamma_{tNN} & -\gamma_{NP} \\ 0 & \gamma_{PN} & -\gamma_{PP} \end{bmatrix}\begin{bmatrix} dN_B \\ dN \\ dN_p \end{bmatrix} + \frac{\Gamma_q \eta_i}{qV}\begin{bmatrix} dI \\ 0 \\ 0 \end{bmatrix}. \tag{5.164}$$

The rate coefficients of the upper left 2×2 submatrix are given by

$$\begin{aligned} \gamma_{BB} &= 1/\tau_s, & \gamma_{BN} &= \Gamma_q/\tau_e, \\ \gamma_{NB} &= 1/\Gamma_q\tau_s, & \gamma_{tNN} &= \Gamma_{NN} + 1/\tau_e. \end{aligned} \tag{5.165}$$

The other rate coefficients are as defined before in Eq. (5.34). Converting to the frequency domain and applying Cramer's rule, we obtain

$$N_{p1}(\omega) = \frac{\Gamma_q \eta_i I_1(\omega)}{qV} \cdot \frac{1}{\Delta_t}\begin{vmatrix} \gamma_{BB} + j\omega & -\gamma_{BN} & 1 \\ -\gamma_{NB} & \gamma_{tNN} + j\omega & 0 \\ 0 & -\gamma_{PN} & 0 \end{vmatrix}, \tag{5.166}$$

can be expressed in terms of the magnitude squared of the electric field in the center of the guide and an effective width, d_{eff}, which accounts for the energy stored in the evanescent fields. Also, for two-dimensional guides in which the lateral width is much wider than the transverse width, we get a similar result.

The time-averaged power propagating in the z-direction is given by

$$P_z = \frac{1}{2}\mathrm{Re}\iint (\mathscr{E} \times \mathscr{H}^*) \cdot \hat{\mathbf{e}}_z \, dx \, dy. \tag{6.6}$$

The electric field, $\mathscr{E}$, is given by Eq. (6.1), and the magnetic field, $\mathscr{H}$, is obtained from the curl of $\mathscr{E}$. We initially consider the TE modes with the electric fields aligned along the y-direction. Because only $\mathscr{E}_y$ and $\mathscr{H}_x$ survive the vector products, and $\mathscr{H}_x = (j/\omega\mu)\partial\mathscr{E}_y/\partial z$, we have

$$P_z = \frac{\beta}{2\omega\mu}\iint |\mathscr{E}_y|^2 \, dx \, dy = \frac{1}{2\eta_g}\iint |\mathscr{E}_y|^2 \, dx \, dy, \tag{6.7}$$

where $\eta_g = \omega\mu/\beta = 377\ \Omega/\bar{n}$ is the waveguide impedance, and

$$\mathscr{E}_y = E_{0m} U_{xm}(x,y) e^{j(\omega t - \beta z)}. \tag{6.8}$$

The form of the transverse mode shape, $U(x,y)$, for the even (symmetric) modes is given by Eqs. (A3.17), (A3.21), and (A3.22) for a rectangular guide cross section.

For simplicity we wish to look at a guide with a lateral width much wider than the transverse width or $w \gg d$. For the lateral dimension we consider only two extreme cases: (a) a fundamental lateral mode or (b) a uniform field. In both cases because w is large, we neglect any fields for $|y| > w$. Thus, the lateral integration gives in case (a),

$$\int_{-\infty}^{\infty} |U(x,y)|^2 dy = |U(x)|^2 \int_{-w/2}^{w/2} \cos^2\left(\frac{\pi}{2w}y\right) dy = |U(x)|^2 \frac{w}{2}, \tag{6.9}$$

(fundamental lateral mode)

and in case (b),

$$\int_{-\infty}^{\infty} |U(x,y)|^2 dy = |U(x)|^2 \int_{-w/2}^{w/2} dy = |U(x)|^2 w. \tag{6.10}$$

(uniform lateral field)

Thus, the lateral integration adds only a multiplication by the width in the case of uniform fields or the half-width for the cosinusoidal lateral mode.

Now, we can plug $U(x)$ from Eqs. (A3.17) and (A3.21) into Eq. (6.7) and perform the integration. For the even modes of a symmetric waveguide,

$$P_z = \frac{w/\rho}{2\eta_g}|E_0 U_0|^2 \left[2\int_0^{d/2} \cos^2(k_{1x}x)\, dx + 2\int_{d/2}^{\infty} \cos^2(k_{1x}d/2) e^{-2\gamma_x(x-d/2)}\, dx\right], \tag{6.11}$$

function between the normalized input field a_1 and the normalized output field b_2,

$$b_2 = S_{21}a_1$$

Converting this structure into a signal flow chart (which is left to the reader as an exercise), we have that

$$\Delta = 1 - \sqrt{1-c^2}e^{-j\tilde{\beta}L_r}.$$

There are two independent forward paths, and one loop in this system, therefore,

$$T_1 \cdot \Delta_1 = \sqrt{1-c^2}e^{-j\tilde{\beta}L_s} \cdot (1 - \sqrt{1-c^2}e^{-j\tilde{\beta}L_r}),$$

and

$$T_2 \cdot \Delta_2 = (jc)^2 \cdot e^{-j\tilde{\beta}L_r} \cdot e^{-j\tilde{\beta}L_s}.$$

Finally, the value for S_{21} is

$$S_{21} = \left(\sqrt{1-c^2}e^{-j\tilde{\beta}L_s} + \frac{(jc)^2 \cdot e^{-j\tilde{\beta}L_r}e^{-j\tilde{\beta}L_s}}{1 - \sqrt{1-c^2}e^{-j\tilde{\beta}L_r}}\right)$$

This result is analogous to the result for a Fabri–Perot cavity, in which the reflection is replaced by $r = \sqrt{1-c^2}$ and transmission by $t = jc$. The pole in the denominator will determine the transfer function of the ring resonator, and this structure can be used as a filter. An example application will be discussed in Chapter 8.

Ring lasers represent an attractive implementation of single mode lasers, due to their simple building blocks and fabrication processes involved. In addition, the "mirrors" in a ring laser are actually light couplers, which allow for a portion of the light to escape the cavity. Figure 6.15 illustrates the use of a directional coupler as an output coupler for a ring laser. In a ring laser, the round trip cavity length is the circumference of the cavity, and there are generally two propagating modes, which are uncoupled (clockwise and counterclockwise), and whose degeneracy must be removed through insertion of differential loss to achieve stable operation. One way to remove the degeneracy, particularly suitable for PIC ring laser implementation is through seeding of a particular mode by an on-chip light source. The priciple of designing a ring laser is illustrated in the following example.

Example 6.7 We wish to analyze a ring laser device as shown in Fig. 6.15, assuming a 4-quantum-well gain region from Fig. 4.31. The passive waveguide cross section in the transverse direction is 0.3 μm thick, and the waveguide index is 3.37. The waveguide is clad by InP, with an index of 3.17 at 1.55 μm. The lateral

region is the same throughout, and there is no significant gap between the laser section and the amplifier section. Assume ideal AR coatings on the output facets, an internal efficiency of 70%, and an internal loss of 15 cm^{-1} throughout. The laser is biased to output 3 mW cw into the amplifier section. We desire the amplifier-modulator to operate as fast as possible, to have a 10 dB optical on/off ratio, and to have an on-level output of 10 mW.

(a) Determine the length and width of the amplifier (same width for laser—cannot exceed 5 μm for single lateral mode).

(b) Determine the total laser current and the on/off level currents to the amplifier.

(c) What is the maximum modulation data rate?

(d) Can the modulation rate be improved for different laser and modulator biases?

3. It is desired to design a quarter-wave-shifted 1.55 μm DFB with a maximum overall power efficiency (power out/power in) at an output power of 10 mW. (Assume a series resistance that scales inversely with active area, which equals 10Ω at an area of 100 μm^2. Estimate the junction voltage by the approximate quasi-Fermi level separation.) At 300 K, we assume a gain as determined by Fig. 4.31, a transverse confinement factor of 6%, an internal efficiency of 70%, an internal loss of 15 cm^{-1}, and a $\kappa = 50\ cm^{-1}$. However, we also empirically decrease the gain curve and the internal efficiency by 1% for each 1°C temperature rise. We assume that the thermal impedance can be estimated by Eq. (2.69) with a substrate thickness, $h = 100$ μm and effective thermal conductivity $\xi = 0.68$ W/cm-°C. Assume lateral cladding is InP.

(a) What length and width is optimum?

(b) Plot the resulting L–I curve.

4. For the sampled grating DBR laser from Example 8.3,

(a) How much current is required on the phase section to tune from one axial mode to the next (assuming a pair of mirror peaks are aligned at some wavelength)?

(b) Assuming that the central mirror peaks and an axial cavity mode are aligned at zero current, what currents are required on the back mirror, the front mirror and the phase section to continuously tune the laser output by exactly 1 nm.

(c) What are the laser threshold current and differential efficiency for tuning currents of both mirrors and the phase section sufficient to change all of the modal indices by 0.005?

5. It is desired to design a 1.55-μm grating assisted codirectionally coupled laser with a tuning enhancement factor of $F = 15$ and a maximum MSR at an output of 5mW. We assume a gain characteristic as in Fig. 4.31, a transverse gain region confinement factor of 6%, an internal efficiency of 70%, $n_{sp} = 1.2, n_{g1} = 4$, an internal loss of 15 cm^{-1} in the active and passive sections of the top guide, an

Eq. (A4.10) to emphasize this modal averaging process. One interesting consequence of this substitution is that if the active region is very thin, and the mode for which we wish to calculate β_{sp} has a null at this point, then $\Gamma_c \approx 0$, from which it follows that $\beta_{sp} \approx 0$ as well. This would not be obvious if we had simply used $1/V_c$ in Eq. (A4.10).

Equation (A4.10) represents the semiclassical version of the spontaneous emission factor. In Chapter 4, a more useful version of the spontaneous emission factor derived from quantum mechanical considerations will be introduced. The quantum version is more general and simpler to evaluate.

READING LIST

Verdeyen JT. *Laser electronics*. 2nd ed. Englewood Cliffs, NJ: Prentice Hall; 1989. Chapter 7.

APPENDIX TWELVE

Threshold Energy for Auger Processes

A12.1 CCCH PROCESS

For the CCCH process in Fig. 4.21, we can write the momentum and energy conservation laws (i.e., initial = final) as

$$\mathbf{k}_1 + \mathbf{k}_2 = \mathbf{k}_3 + \mathbf{k}_4, \tag{A12.1a}$$

$$\Delta E_1 + \Delta E_2 = -(E_g + \Delta E_3) + \Delta E_4, \tag{A12.1b}$$

where the $\mathbf{k}$'s are vectors in k-space, and E_c has been used as the energy reference level in the latter equation. Rearranging the energy conservation law, we find

$$\Delta E_4 - E_g = \Delta E_1 + \Delta E_2 + \Delta E_3. \tag{A12.2}$$

From Eq. (4.107b), it follows that the most probable transition corresponds to the minimum possible energy of state 4. This minimum value for ΔE_4 is referred to as the *threshold* energy, E_T, of the Auger process.

To determine the threshold energy, we need to minimize Eq. (A12.2). If we assume that all bands are parabolic, we can set $\Delta E_i \propto \mathbf{k}_i \cdot \mathbf{k}_i / m_C$ for the three conduction band states and $\Delta E_3 \propto \mathbf{k}_3 \cdot \mathbf{k}_3 / m_H = \mu \mathbf{k}_3 \cdot \mathbf{k}_3 / m_C$, for the valence band where $\mu = m_C / m_H$. At the minimum, ΔE_4 will be independent of variations

Diode Lasers and Photonic Integrated Circuits, Second Edition.
Larry A. Coldren, Scott W. Corzine, and Milan L. Mašanović.

First, we multiply the complex conjugate of the transverse wave equation, Eq. (6.5), by ΔU to get

$$\Delta U(\nabla_T^2 U^*) + \Delta U[\varepsilon^*(x,y,z)k_0^2 - \beta^{*2}]U^* = 0. \tag{A14.1}$$

Thus, the last two terms in the last integral in Eq. (A14.1) can be replaced by $-\Delta U(\nabla_T^2 U^*) + (\varepsilon - \varepsilon^*)k_0^2 U^* - (\beta^2 - \beta^{*2})U^*$. If ε and β were real, then we would only need $-\Delta U(\nabla_T^2 U^*)$. Making the replacement,

$$\begin{aligned}\int &[(\nabla_T^2 \Delta U)U^* + \varepsilon k_0^2 \Delta U U^* - \beta^2 \Delta U U^*]\, dA \\ &= \int [(\nabla_T^2 \Delta U)U^* - \Delta U(\nabla_T^2 U^*)]\, dA \\ &\quad + \int [(\varepsilon - \varepsilon^*)k_0^2 \Delta U U^* - (\beta^2 - \beta^{*2})\Delta U U^*]\, dA. \end{aligned} \tag{A14.2}$$

Now, the first integral on the right is identically zero because

$$\begin{aligned}\int [(\nabla_T^2 \Delta U)U^* - \Delta U(\nabla_T^2 U^*)]\, dA &= \int \nabla_T \cdot [(\nabla_T \Delta U)U^* - \Delta U(\nabla_T U^*)]\, dA \\ &= \oint_\infty \hat{\mathbf{e}}_n \cdot [(\nabla_T \Delta U)U^* - \Delta U(\nabla_T U^*)]\, ds \equiv 0. \end{aligned} \tag{A14.3}$$

The latter equality uses Green's Theorem to convert the integral over the cross-sectional area to a line integral around the perimeter of the cross section (in this case, at infinity). The vector $\hat{\mathbf{e}}_n$ is the unit vector normal to the contour of integration. The contour integral at infinity is zero because both U and ΔU must vanish at infinity for any guided mode. The second integral on the right side of Eq. (A14.2) also is identically zero for ε and β real. In fact, even for complex ε and β, it tends to be negligible in comparison to the first integral on the right side of Eq. (A14.1) in most cases, since $\Delta U \ll U$, and because the loss or gain of the unperturbed problem can usually be chosen to be sufficiently small. Only in the extreme case where the gain provides most of the waveguiding effect (as in gain-guided lasers) will this term be nonnegligible. In this rare case, the use of the $\Delta\beta$ formula is questionable.

READING LIST

Haus HA. *Waves and fields in optoelectronics*. Englewood Cliffs, NJ: Prentice Hall; 1984.

Supplement to Fig 1.9; p 15

From 1st Edition

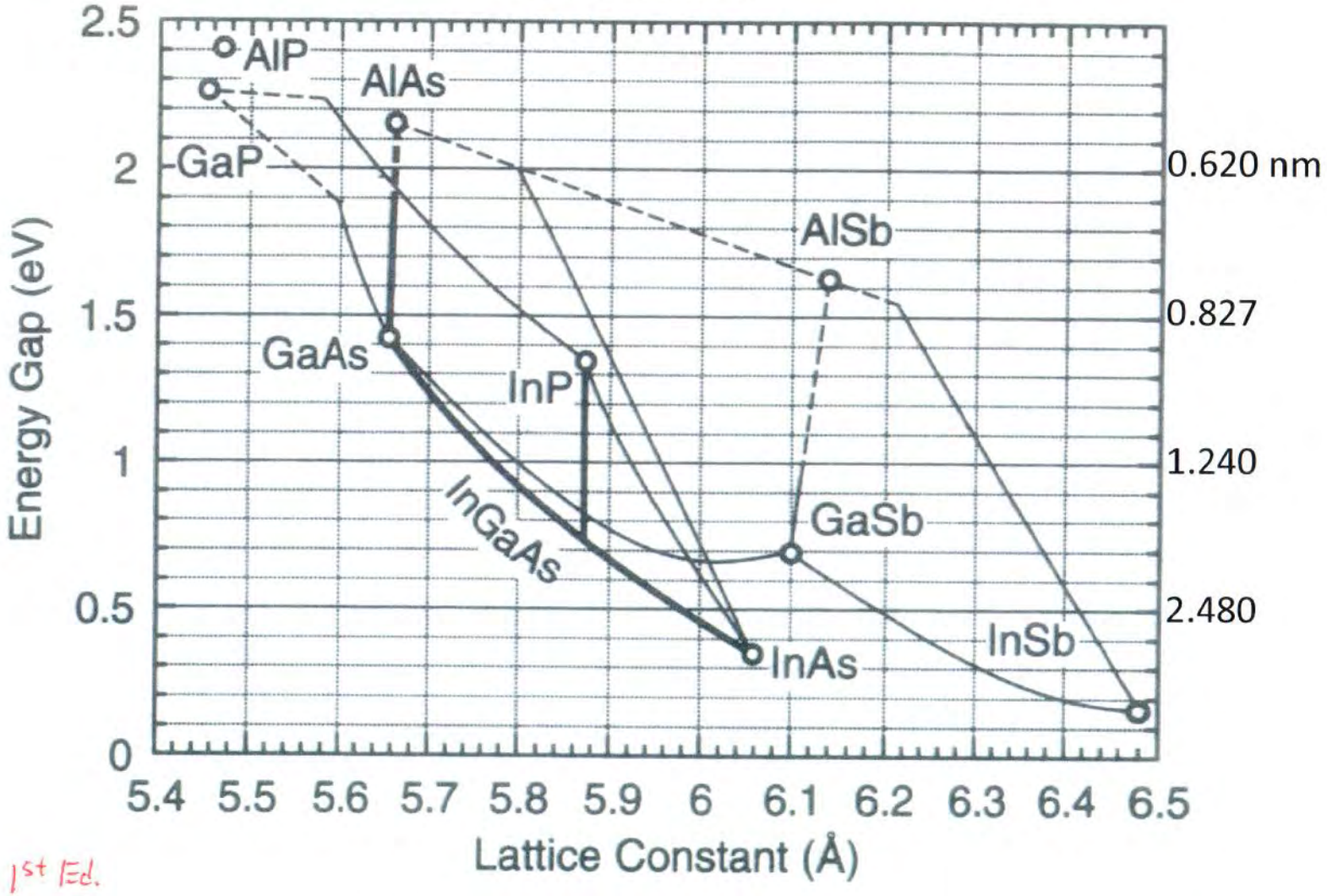

1st Ed.

FIGURE 1.6 Energy gap vs. lattice constant of ternary compounds defined by curves that connect the illustrated binaries.